



MONASH
University

Honours Report

**Generating Gravitational Wave Signals From
Machine Learning and Numerical Relativity**

Paul Easter

Supervisors: Paul Lasky, Andrew Casey
Monash University School of Physics and Astronomy

November 8, 2017

Abstract

Detection of gravitational waves from the remnant of a binary neutron star merger will require the generation of a large bank of template waveforms. Numerical relativity methods can generate gravitational wave strain waveforms, but this process is computationally intensive taking around 100,000 CPU hours per waveform. We investigated using machine learning algorithms to assist in this task. We initially used principal components analysis, an unsupervised learning algorithm on frequency scaled and frequency unscaled data. This was to obtain an intuitive idea of the data involved and to determine which data we wished to use for the supervised machine learning tasks. We then implemented the machine learning algorithm The Cannon 2 with unscaled frequency data and used this to predict output spectra. This algorithm performed reasonably well without cross-correlation, but the residual SNR of the reconstructed signals ranged from 3.0 to 25.0 when leave one out cross validation was implemented. The goal for the residual SNR was less than 1.0. We finally implemented a random forest machine learning algorithm, which performed well in predicting the output spectrum, with residual SNR varying from 0.6 to 1.5. This was not implementing leave one out cross validation though, and could not be directly compared to the results from The Cannon 2. However, these training and prediction algorithms are fast, taking only a few seconds to operate on all 25 waveforms.

Contents

Abstract	2
1 Introduction	6
2 General relativity	6
2.1 Gravitational waves	7
2.1.1 Generation of Gravitational Waves	7
2.1.2 Detection of Gravitational Waves	8
3 Neutron stars mergers	11
3.1 Time evolution of binary neutron stars	11
3.2 Binary neutron star inspiral	13
3.3 Observational binary neutron star masses	13
3.4 Neutron star equation of state	14
3.4.1 Other binary neutron stars parameters	16
4 Numerical general relativity	19
4.1 Template requirements	20
4.2 Supplied data	20
5 Machine learning	23
5.1 Over fitting	24
5.2 Cross-validation	24
5.3 Comparison metric	25
5.3.1 Frequency dependent metrics	25
5.4 Principal components analysis	25
5.5 Preprocessing of data	26
5.6 The Cannon 2 setup	27
5.6.1 Implementation	27
5.7 Random forest	27
5.8 Waveform preparation	28
5.9 Numerical relativity waveforms	28
6 Results	29
6.1 Principal components analysis	29
6.1.1 Scaled Frequency	29
6.1.2 Unscaled Frequency	33
6.1.3 Principal components summary	37

6.2	The Cannon analysis	37
6.2.1	Entire training set	38
6.2.2	Leave one out cross-validation	40
6.2.3	Training on real and imaginary components of the Fourier transform of the signals	43
6.3	The Cannon 2 summary	45
6.4	Random forest analysis	47
6.4.1	Inferred waveforms	47
6.4.2	Random forest summary	52
7	Future tasks	53
8	Conclusion	53
9	Acknowledgements	53
References		54

List of Figures

1	Time evolution of the h_x (top) and h_+ (bottom) polarisations of the gravitational strain. Time progresses left to right, from a) $t = 0$, $\theta = 0$ to e) $t = T$, $\theta = \omega T = 2\pi$, where T is the period and θ is the phase of the gravitational wave strain.	7
2	An aerial image of the LIGO facility in Hanford, Washington.	9
3	The sky localisation for GW170814 with LIGO and Virgo.	9
4	Gravitational wave chirp from GW170817.	10
5	Design sensitivity for LIGO and Virgo.	11
6	Evolutionary paths of BNS mergers.	12
7	Mass-radius diagram of neutron stars from Demorest et al. (2010). The most massive observed neutron star at the time of this publication was J1614-2230 with a mass of $1.97 \pm 0.04 M_\odot$. This quantity is shown by the thickest horizontal line. Three categories of EOS are shown. Nucleon EOS in blue, and strange quark matter EOS in green. The EOS marked in pink consist of nucleons and hyperons (GM3), or nucleons and kaons (GS1) (Lattimer & Prakash, 2001).	16
8	Plot of simulated $h_+(t)$ waveforms at 50Mpc.	21
9	Frequency response of the simulated waveforms at 50Mpc.	22
10	Block diagram of supervised machine learning algorithm.	23
11	Plot indicating underfitting, good fitting, and overfitting.	24
12	Schematic showing the relative importance of adjacent principal components.	26
13	Three component PCA of the frequency scaled fourier transform amplitude.	30
14	Three component PCA of the frequency scaled fourier transform amplitude projected onto two dimensions.	31
15	Three component PCA of the frequency scaled fourier transform phase.	32
16	Three component PCA of the frequency scaled fourier transform phase projected onto two dimensions.	33
17	Three component PCA of the unscaled fourier transform amplitude.	34

18	Three component PCA of the unscaled fourier transform amplitude projected onto two dimensions.	35
19	Three component PCA of the unscaled fourier transform phase.	36
20	Three component PCA of the unscaled fourier transform phase projected onto two dimensions.	37
21	The Cannon frequency response of waveform APR4-q10-M1275.	38
22	The Cannon frequency response of waveform ALF2-q10-M1225.	39
23	The Cannon LOOCV frequency response of waveform APR4-q10-M1275.	40
24	The Cannon LOOCV frequency response of waveform ALF2-q10-M1225.	41
25	The Cannon LOOCV histogram of residual SNR.	42
26	The Cannon LOOCV histogram of residual SNR excluding outliers	42
27	The Cannon complex frequency response of waveform APR4-q10-M1275 trained on real and imaginary signals.	44
28	The Cannon complex frequency response of waveform ALF2-q10-M1225 trained on real and imaginary signals.	45
29	Frequency and time response for random forest regression of waveform APR4-q10-M1275.	47
30	Frequency and time response for random forest regression of waveform ALF2-q10-M1225.	48
31	Histogram for the residual SNR of the random forest regression.	49
32	Mean histogram for the residual SNR of the random forest regression for 20 random values.	49
33	Box plot of the random forest residual SNR for 100 random values sorted by EOS and mass.	50
34	Box plot of the random forest residual SNR for 100 random values sorted by mean residual SNR.	51
35	Relative importance of labels, random forest without cross validation.	52

List of Tables

1	Known masses of binary neutron systems and possible binary neutron systems.	14
2	Table showing the polytropic constants used neutron star EOS.	15
3	Parameters for waveforms: M_{TOV} , M_{total} , R_{TOV} , \bar{R} , M_1 , M_2 , \bar{M} , q , κ_2^T .	17
4	Parameters for waveforms: C , J , M_{ADM} , M_b , \bar{k}_2 , M_{ol} , $\bar{\Lambda}$, f_{cont} , f_{peak-j} .	18

1 Introduction

The detection of gravitational-waves from the merger of two black holes in 2015 (Abbott et al., 2016b) heralded the onset of a new method of investigating the known universe. Since then there has been a number of other detections of binary black hole coalescences (Abbott et al., 2016a, 2017a,b). Furthermore, a binary neutron star (BNS) merger was detected on 17th August 2017 (Abbott et al., 2017c) generating renewed interest in the properties of neutron stars.

The properties of matter in the extreme environment of neutron stars is not well known, models have been generated that predict the behaviour of matter in this state using particular equations of state (EOS) . There are several competing EOS that could describe the true behaviour of neutron star matter, but at this point in time, it is not known which EOS represents the best model of extreme matter. The detection of gravitational-waves from a binary neutron star post-merger remnant could supply enough information to, at the very least, narrow down the EOS options significantly, and possibly determine a favoured model.

This becomes more likely as advanced LIGO and Virgo reach design sensitivity (see section 2.1.2) in coming years and detections of the BNS events increase in rate. To be able detect the post-merger remnant for BNS, LIGO and Virgo require a large bank ($\sim 10^5 - 10^6$) of template waveforms covering all possible combinations of potential EOS and neutron star parameters. A detection trigger would then be generated if an incoming gravitational-wave signal matches one of the template signals. The waveforms required for these templates are generated by numerical relativity simulations which are computationally intensive. Each waveform takes approximately 100,000 CPU hours to generate (Takami et al., 2015). This excludes the possibility of generating the large banks of template waveforms in this manner.

This thesis aims to address this critical problem by using a combination of the numerical relativity and machine learning signals to generate large banks of template waveforms. To this end we performed principal component analysis on the Fourier transforms (section 6.1) of a set of numerical relativity waveforms to see if we could obtain any useful information to aid in the machine learning process . We then used a learning algorithm called The Cannon 2, to see if we could accurately reconstruct signals (6.2). We then utilised another learning algorithm known as random forest to attempt to reconstruct the original numerical relativity waveforms (sec:RandomForest).

2 General relativity

The extreme matter of neutron star collisions is determined by general relativity. General relativity defines the relationship between space-time and mass-energy. In general relativity, gravitational changes are propagated at the speed of light, whereas in Newtonian gravity these changes are considered instantaneous. The presence of large masses generate curvature in space-time as dictated by Einstein's equation, shown here in natural units with $c = G = 1$.

$$G_{\mu\nu} = R_{\mu\nu} - \frac{1}{2}Rg_{\mu\nu} = 8\pi T_{\mu\nu}. \quad (1)$$

The left hand side of equation 1 represents the curvature of space-time, $G_{\mu\nu}$, which is composed of the Ricci curvature tensor $R_{\mu\nu}$, the Ricci scalar, R , and the space-time metric, $g_{\mu\nu}$. The stress energy tensor, $T_{\mu\nu}$, represents the presence of mass, energy, and pressure. In the absence of matter, the metric of space-time is represented by the Minkowski metric of special relativity and Einstein's equation vanishes. The formulation of general relativity allows for

the existence of gravitational-waves (section 2.1) and modifies the analysis of neutron stars, particular the equation of state (section 3.4). This in turn determines the outcome from merger scenarios (section 3) and increases the computational intensiveness of BNS merger simulations (section 4).

2.1 Gravitational waves

By analysing linear perturbations of $G_{\mu\nu}$ in flat space ($T_{\mu\nu} = 0$), the following equation can be constructed (eg Flanagan & Hughes (2005)):

$$\left(-\frac{\partial^2}{\partial t^2} + \nabla^2 \right) \bar{h}_{\alpha\beta} = 0, \quad (2)$$

where \bar{h} is the trace reversed transformation of the perturbation of flat space, h . The solutions of equation 2 are plane waves propagating at the speed of light. Converting this to a transverse traceless representation allows the determination of the gravitational-wave strain polarisation components h_+ and h_\times for a wave propagating in the z direction (eg Flanagan & Hughes (2005)):

$$h_{xx}^{TT} = -h_{yy}^{TT} \equiv h_+ (t - z), \quad (3)$$

$$h_{xy}^{TT} = h_{yx}^{TT} \equiv h_\times (t - z), \quad (4)$$

where all other components of $h_{\mu\nu}^{TT}$ are zero. Figure 1 shows how the space is stretched and compressed over time as a gravitational-wave passes by.

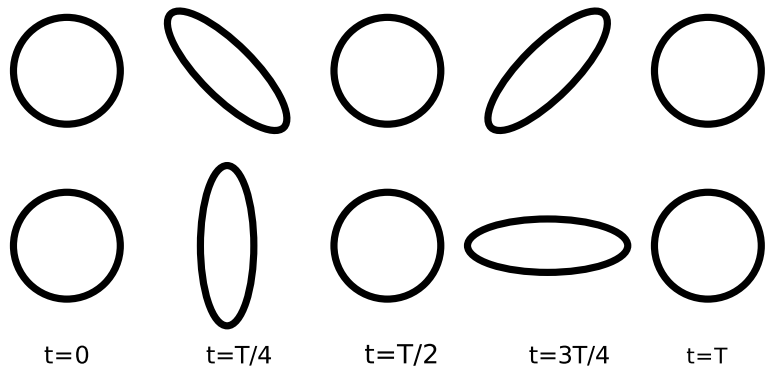


Figure 1: Time evolution of the h_\times (top) and h_+ (bottom) polarisations of the gravitational strain. Time progresses left to right, from a) $t = 0$, $\theta = 0$ to e) $t = T$, $\theta = \omega T = 2\pi$, where T is the period and θ is the phase of the gravitational wave strain.

2.1.1 Generation of Gravitational Waves

The second moment of the mass distribution is the smallest possible moment required to generate gravitational-waves (eg Flanagan & Hughes (2005)). The zeroth moment consists of the total mass of the system, which is conserved, and the dipole moment consists of total angular momentum of the system, which is also conserved. For a slow moving mass, the

perturbation of flat space, h^{TT} , generated from the second moment can be written as (eg Carroll (2004)):

$$h_{ij}^{TT} = \frac{2}{r} \frac{d^2 J_{ij}^{TT} (t-r)}{dt^2}, \quad (5)$$

where J^{TT} is the transverse traceless representation of the second moment and is known as the reduced quadrupole moment tensor, $t-r$ is the retarded time and r is the distance from the observer to the system. The time derivatives of the quadrupole moment for an axisymmetric rotating object is zero, so gravitational-waves are produced only by non-axisymmetric rotation. To get a feel for the magnitude of h , equation 5 can be redimensionalised to:

$$h_{ij}^{TT} = \frac{2G}{rc^4} \frac{d^2 J_{ij}^{TT} (ct-r)}{dt^2}. \quad (6)$$

The magnitude of the perturbation in equations (5) and (6) goes as the inverse of distance, as does its components, the gravitational-wave strain. This can be compared to electromagnetic radiation, which goes as the square of the distance, implying that gravitational-wave energy may be more dominant. However, the presence of G/c^4 significantly reduces the magnitude of the gravitational-wave strain. An order of magnitude approximation for the gravitational-wave strain amplitude for the merger two neutron stars can be calculated using dimensional analysis, by assuming a distance of $r = 100\text{Mpc}$, a mass of $1M_\odot$, with $R = 100\text{km}$ to the centre of mass. Dimensionally J is in units of $MR^2 \sim 1M_\odot \cdot (100\text{km})^2$. Taking the second time derivative is approximately equal to dividing J by the square of the system period. Using Kepler's law to approximate the period $T^2 \sim \frac{4\pi^2 R^3}{GM_\odot} \sim \frac{(100\text{km})^3}{GM_\odot}$ gives:

$$h \sim \frac{G}{100\text{Mpc} \cdot c^4} \frac{M_\odot (100\text{km})^2}{T^2} \sim \frac{G^2 M_\odot^2}{(100\text{Mpc})(100\text{km}) \cdot c^4} \sim 10^{-23}. \quad (7)$$

If this strain were measured over a distance of 1m, then the change in distance measured due to this gravitational-wave would be 10^{-23} m. In comparison, the radius of a proton is 10^{-15} m so the strain is small.

2.1.2 Detection of Gravitational Waves

Even though the size of the strain for a gravitational-wave is so small, both the LIGO and Virgo observatories have successfully detected merger events. Gravitational waves were first detected by LIGO, the **L**aser **I**nterferometer **G**ravitational **W**ave **O**bservatory. LIGO consists of two L shaped interferometers with arms four kilometres long. One interferometer is located in Hanford (Washington, U.S.A.) and the other in Livingston (Louisiana, U.S.A). Figure 2 shows an aerial view of the Hanford facility.



Figure 2: An aerial image of the LIGO facility in Hanford, Washington showing the two long interferometer arms (Caltech/MIT/LIGO Lab, 2015).

The two facilities are approximately 3700 km apart which allows a limited localisation of the source in the sky by triangulation of the gravitational-wave signal. The first three gravitational-wave detections were designated GW150914 (Abbott et al., 2016b), GW151226 (Abbott et al., 2016a) and GW170104 (Abbott et al., 2017a), detected on September 14 2015, December 26 2015 and January 4 2017 respectively. Each event represented the merger of two black holes. On the 1st of August 2017 the Virgo observatory, located near Pisa (Italy), joined LIGO for observations until the 25th of August, when LIGO was turned off for system upgrades. The interferometer arms of the Virgo observatory are 3 km long, making it less sensitive than both LIGO observatories, with 4km interferometer arms. However, having three independent observations of a gravitational-wave event has distinct advantages in sky localisation. On the 14th of August 2017, all three observatories detected a binary black hole merger, GW170814, with a significantly reduced the sky localisation as can be seen in figure 3.

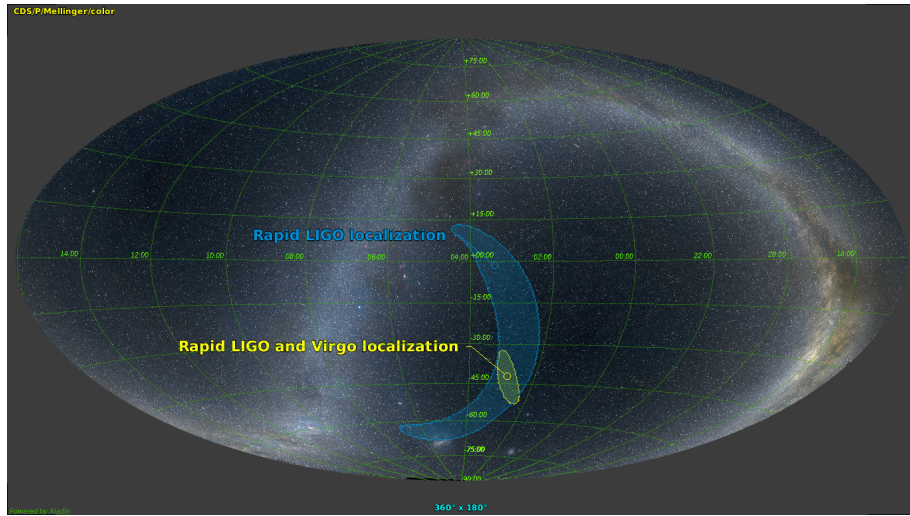


Figure 3: The sky localisation for GW170814 with LIGO only is shown in blue, whereas the sky localisation with Virgo included is shown in yellow. The localisation with Virgo operating is significantly less (the Virgo Collaboration, 2017).

The sky localisation of the two LIGO observatories is shown in blue and covers a large

part of the sky map, however, when data from Virgo is also considered then the sky map reduces to the area specified in yellow. This is an important factor if we are able to detect a binary neutron star merger, as electromagnetic observatories would want to observe the binary neutron star merger as soon as possible.

On the 17th of August 2017 the LIGO, Virgo collaboration detected the inspiral of a binary neutron star for the very first time (Abbott et al., 2017c). Due to the improved sky localisation achieved with the inclusion of Virgo, electromagnetic observatories were able to pin point the host galaxy and merger location. The gravitational-wave signal detected is shown in figure 4.

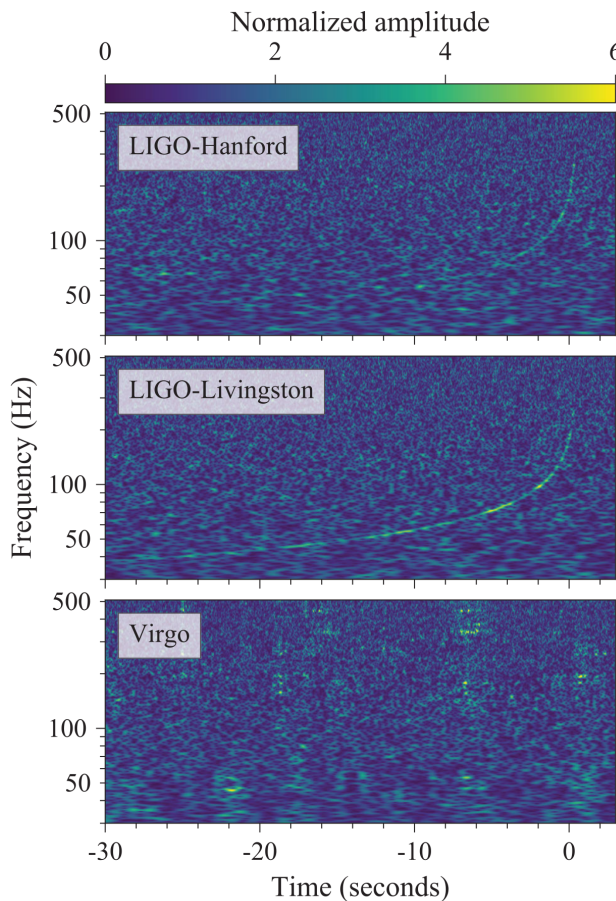


Figure 4: Frequency response of the gravitational strain versus time for LIGO-Hanford (top), LIGO-Livingston (middle), and Virgo (bottom). A characteristic chirp generated by the gravitational waves of the neutron star merger process is visible in the top two panels. Virgo was determined to be in the null of the antenna pattern for this gravitational-wave signal, so chirp was seen (from Abbott et al., 2017c).

Figure 4 shows the chirp signal detected at both LIGO facilities but no signal in Virgo. The signal was not visible in Virgo due to the influence of the antenna pattern of the interferometer however, this still led to a reduced sky location of 28 deg^2 (90% probability) (Abbott et al., 2017c). Furthermore, it is expected that as LIGO and Virgo increase their sensitivity towards design sensitivity, then the incidence of BNS mergers will increase as well. Figure 5 shows the expected progression of BNS sensitivity over time for both LIGO and Virgo.

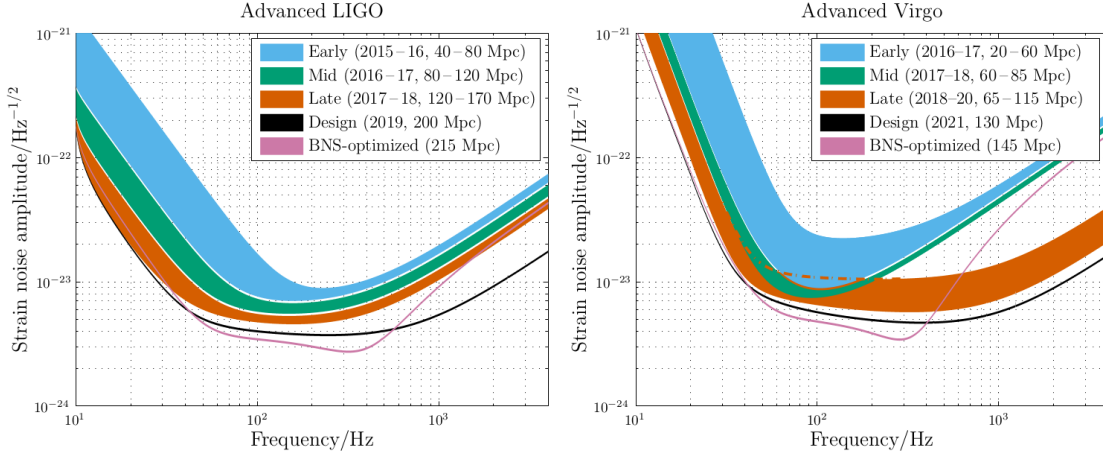


Figure 5: Expected design sensitivity for LIGO and Virgo with respect to the detection of binary neutron stars from Abbott et al. (2016c). As time progresses, both observatories will improve the detection capabilities until reaching design sensitivity. LIGO is predicted to reach design sensitivity in 2019 and will be able to detect BNS mergers out to ~ 200 Mpc. The vertical axis is the strain noise amplitude in units of $\text{Hz}^{-1/2}$, and the horizontal axis is the frequency in Hz .

For post-merger detection of BNS signals, the frequency range of interest is around 1000-4000Hz (section 4.2). At this frequency range the amplitude spectral noise density ranges from $\sim 5 \times 10^{-24} - 2 \times 10^{-23}$ for LIGO and Virgo at design sensitivity.

3 Neutron stars mergers

Neutron stars mergers are of interest in several fronts: their mergers are believed to be responsible for the generation of short gamma ray bursts (eg Narayan et al. (1992); Rezzolla et al. (2011); Ruiz et al. (2016)) and subsequent x-ray afterglows; the mergers can be a source of gravitational-waves, black holes, and highly magnetised massive neutron stars. Neutron star mergers have also been suggested as a source of nucleosynthesis of neutron rich elements (eg Symbalisty & Schramm (1982); Arnould et al. (2007)). Binary neutron star mergers potentially allow determination of the neutron star equation of state, through observation of the x-ray after-glow following gamma ray bursts (Lasky et al., 2014). The gravitational-waves emitted from a BNS merger hold information about the extreme states of matter generated in such an event and can shed information on the physical models used to describe these states. This section will investigate the time evolution of BNS (section 3.1), the inspiral process that leads toward BNS merger (section 3.2), the maximum mass value for neutron stars (section 3.3), the neutron star equation of state (section 3.4)

3.1 Time evolution of binary neutron stars

Binary neutron stars will eventually coalesce due to the emission of gravitational-waves. The emitted gravitational-waves carry away energy of the system, leading to a decrease in separation between the orbits and a corresponding increase in the orbital frequency (see section 3.2). The physics of the merging process is shown in the simplified schematic shown in figure 6 (Baiotti & Rezzolla, 2017).

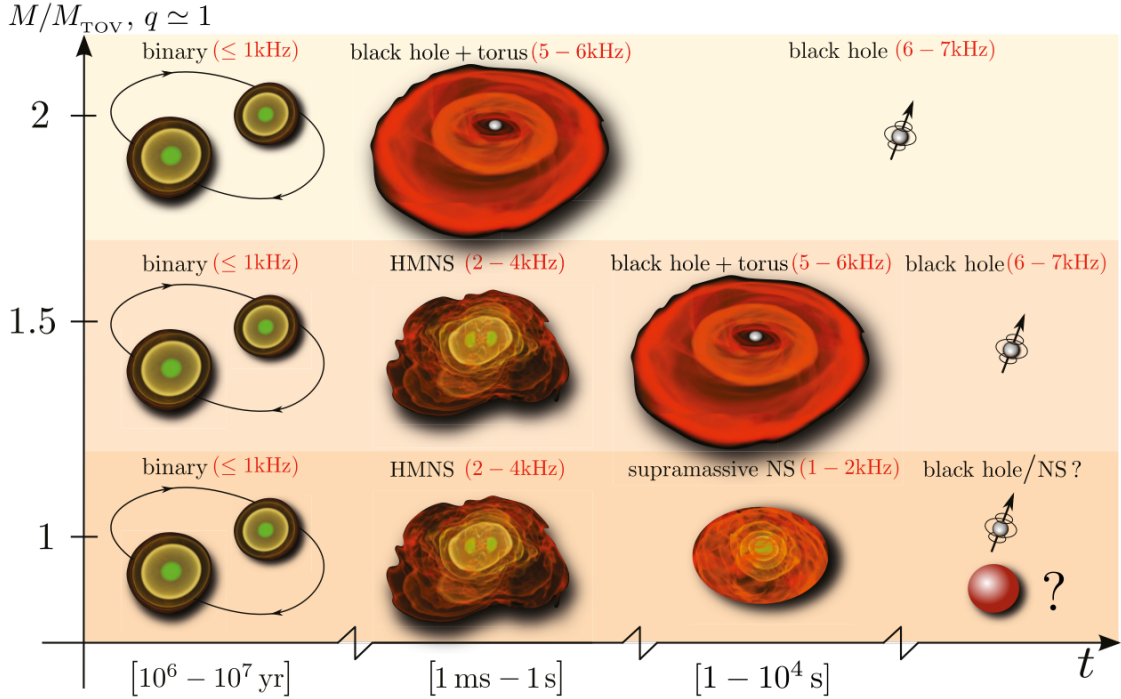


Figure 6: Possible evolutionary paths of BNS mergers (from Baiotti & Rezzolla (2017)). The vertical axis shows the ratio of the total mass to M_{TOV} , the horizontal axis shows the characteristic time. The mass of each neutron star is approximately equal ($q \simeq 1$). If the total mass is around $\gtrsim 1.5M_{TOV}$ then, after merging, the neutron stars form a black hole directly. If the total mass is ~ 1 to $1.5M_{TOV}$, then a hypermassive neutron star can form, with excess angular momentum preventing immediate collapse. After the excess angular momentum is dissipated, the system will evolve into a black hole, or a supramassive neutron star, depending on the final mass of the system. As the rigidly rotating supramassive neutron star dissipates its angular momentum, it will collapse into either a neutron star or a black hole, depending on whether the final mass is larger than M_{TOV} . When a black hole is formed, there may initially be surrounding material which will be shaped in a toroidal configuration. The frequency of the gravitational waves emitted by the system at various stages is shown in red parenthesis.

The vertical axis shows the total mass of the system in units of M_{TOV} , with M_{TOV} in turn dependent on the EOS (see section 3.4). The variable q is the ratio of the component masses and is set to approximately one for these plots, implying that each neutron star component has around the same mass. The top row of figure 6 shows the merger process of two equal mass neutron stars with a total mass of $\gtrsim 1.5M_{TOV}$. In this scenario a black hole will be formed immediately with a hot toroidal shaped accretion disc. The accretion disc can survive for around 1-10 seconds before accreting onto the final black hole remnant.

The second row of figure 6 shows the merger process for a total mass of around $1.5M_{TOV}$. In this scenario, a hypermassive neutron star (HMNS) is formed. A HMNS is supported by centrifugal forces due to differential rotation. The mass of the HMNS is larger than the maximum mass (M_{MAX}) allowable for a uniformly rotating neutron star which has been shown by Breu & Rezzolla (2016) to be $(1.203 \pm 0.022)M_{TOV}$. As the angular momentum is dissipated, the centrifugal support is lost through magnetic braking and the HMNS collapses into a black hole with a toroidal disc, which in turn is accreted onto the black hole.

The final row of figure 6, with a total mass around $1M_{TOV}$ initially follows the same evolutionary path as the $1.5M_{TOV}$ system, resulting in a differentially rotating supramassive

neutron star (SMNS). However, as centrifugal support is lost it may directly form: 1) a rotating neutron star if $M < M_{TOV}$, or 2) a rigidly rotating supramassive neutron star (SMNS) if $M > M_{TOV}$. A SMNS is quasi-stable by virtue of its rotation with lifetimes varying from 10s to 4.4×10^4 s (Ravi & Lasky, 2014) resulting either in a enduring SMNS or collapse into a black hole.

3.2 Binary neutron star inspiral

As stated in section 3.1, BNS systems lose energy due to the emission of gravitational-waves, this energy loss due can be calculated for a binary system of equal mass (Carroll, 2004, chap 7.5-7.6). With mass, M , and separation, a , in a quasi-circular orbit, the energy loss, \dot{E} , is given by:

$$\dot{E} = -\frac{64M^5}{5a^5}. \quad (8)$$

The corresponding change in separation is given by:

$$\dot{a} = -\frac{128M^3}{5a^3}. \quad (9)$$

Equation (9) can be integrated to give the lifetime of the binary:

$$t_{BINARY} = \frac{5a^4}{512M^3}. \quad (10)$$

The lifetime to merge calculation in equation 10 is a critical number for detecting BNS mergers. If the initial separation is too large then the time to merge will become larger than the age of the universe. The relationship in equation 10 is equally valid for binary black hole mergers and experimental evidence exists showing the decreasing gravitational-wave strain period leading up to the merger, as shown in figure 4. As the BNS orbital period decreases, the gravitational-wave frequency increases leading to the characteristic chirp signal seen in both the time response and frequency spectrum.

3.3 Observational binary neutron star masses

It is important to consult the observational evidence for the masses of neutron stars before looking into the specific neutron star equations of state and other parameters. The most massive neutron stars measured to date are PSR J1614-2230 with a mass of 1.97 ± 0.04 M_\odot (Demorest et al., 2010) and PSR J0348+0432 with a mass of 2.01 ± 0.04 M_\odot (Antoniadis et al., 2013). The masses of other known neutron stars in binary pulsar systems are shown in table 1:

System	M_T (M_\odot)	M_{psr} (M_\odot)	M_c (M_\odot)
Systems with well-measured component masses			
J0453+1559	2.734 (4)	1.559 (5)	1.174 (4)
J0737–3039	2.58708 (16)	1.3381 (7)	1.2489 (7) y
B1534+12	2.678463 (8)	1.3330 (4)	1.3455 (4)
J1756–2251	2.56999 (6)	1.341 (7)	1.230 (7)
J1906+0746	2.6134 (3)	1.291 (11) y	1.322 (11) ?
B1913+16	2.828378 (7)	1.4398 (2)	1.3886 (2)
B2127+11C g	2.71279 (13)	1.358 (10)	1.354 (10)
Systems with total binary mass measurement only			
J1518+4904	2.7183 (7)	<1.768	>0.950
J1811–1736	2.57 (10)	<1.64	>0.93
J1829+2456	2.59 (2)	<1.34	>1.26
J1930–1852	2.59 (4)	<1.32	>1.30

Table 1: Known masses of binary neutron systems and possible binary neutron systems (modified from Özel & Freire (2016)). The top seven pulsars have well measured masses, whereas the lower four have bounds on the component masses only. In all cases the total mass is well known. The total system mass is M_T , the mass of the first component is M_{psr} , the mass of the second component is M_c . Annotations: g) systems in globular clusters, y) normal nonrecycled radio pulsars, ?) companion may not be a neutron star.

The component mass ratio, $q = M_{psr}/M_c$, is within 10% of unity for the first seven systems in table 1, with the exception of the first system, J0453+1559. This seems to suggest that equal mass binary neutron stars may be probable than unequal mass systems. The first system, J0453+1559, being the exception, with a mass ratio of 1.33.

3.4 Neutron star equation of state

With the maximum observational mass known in section 3.3, it is now possible to look at the models that are used to determine the properties on neutron stars. The properties of a neutron star can be simulated from the four Tolman-Oppenheimer-Volkoff (TOV) equations, together with polytropic equation relating the pressure to the density, specify the physics of neutron stars. The TOV equations are spherically symmetric solutions to equation 1 and are defined as (eg Shapiro & Teukolsky, 2004, Ch 5.7):

$$e^{2\lambda} = \left(1 - \frac{2m}{r}\right)^{-1}, \quad (11)$$

$$\frac{dm}{dr} = 4\pi r^2 \rho, \quad (12)$$

$$\frac{dP}{dr} = -\frac{\rho m}{r} \left(1 + \frac{P}{\rho}\right) \left(1 + \frac{4\pi P r^3}{m}\right) \left(1 - \frac{2m}{r}\right)^{-1}, \quad (13)$$

$$\frac{d\Phi}{dr} = -\frac{1}{\rho} \frac{dP}{dr} \left(1 + \frac{P}{\rho}\right)^{-1}, \quad (14)$$

where m is the mass/energy contained within radius r . The mass, energy density is given by ρ , and the pressure is designated as P . The polytropic equation defines $P(\rho) = f(\rho)$ depending on the underlying assumptions on the physics of the neutron star. Given the central pressure, equations (12) and (13) can be integrated from $r = 0$ until $P(r) = 0$, which then defines the neutron star's radius, $R = r$ and mass, $M = m(r)$.

The polytropic constants used for the EOS that are used in this project are shown in table 2:

EOS	N	Γ_2	Γ_3	Γ_4	ρ_1 [g/cm ³]	M_{\max} [M_{\odot}]	R_{\max} [km]
GNH3	4	2.664	2.194	2.304	6.66038×10^{13}	1.9768	11.266
H4	4	2.909	2.246	2.144	8.87824×10^{13}	2.0282	11.603
ALF2	4	4.070	2.411	1.890	1.94771×10^{14}	1.9911	11.308
SLy	4	3.005	2.988	2.851	1.46231×10^{14}	2.0606	9.9349
APR4	4	2.830	3.445	3.348	1.51201×10^{14}	2.2000	9.8733

Table 2: Table edited from Takami et al. (2015) showing the polytropic constants used for the neutron star EOS in numerical analysis. Also shown is the mass and radius corresponding to the maximum TOV mass. Additional parameters are $K = 123.647$, $K_1/c^2 = 3.99873692 \times 10^{-8}$ (g/cm³)^{1- Γ_1} , $\Gamma_1 = 1.35692395$, $\rho_2 = 5.01187237 \times 10^{14}$ g/cm³, $\rho_3 = 10^{15}$ g/cm³.

With this information available, it becomes possible to generate mass-radius loci for various EOS. Figure 7 shows a plot of the mass radius diagram of neutron stars with various equations of state. There are three types of EOS in this diagram, the blue curves are derived from EOS determined from nucleons, the pink curves are derived from nucleons and hyperons (GM3), or nucleons and kaons (GS1), and the green curves are from strange quark matter:

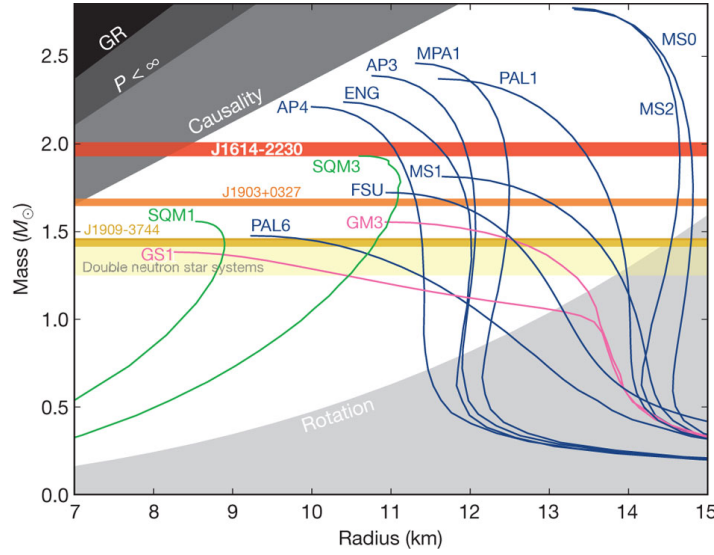


Figure 7: Mass-radius diagram of neutron stars from Demorest et al. (2010). The most massive observed neutron star at the time of this publication was J1614-2230 with a mass of $1.97 \pm 0.04 M_{\odot}$. This quantity is shown by the thickest horizontal line. Three categories of EOS are shown. Nucleon EOS in blue, and strange quark matter EOS in green. The EOS marked in pink consist of nucleons and hyperons (GM3), or nucleons and kaons (GS1) (Lattimer & Prakash, 2001).

For each EOS in figure 7 there is a corresponding maximum stable mass (top left of each curve) corresponding to the TOV mass (M_{TOV}). The TOV mass determines the maximum non-rotating mass that a neutron star can possess. Any non-rotating neutron star with a mass exceeding M_{TOV} will gravitationally collapse to a black hole due to radial instabilities. The maximum observed neutron star mass to date is approximately $2 M_{\odot}$ (Antoniadis et al., 2013; Demorest et al., 2010) (section 3.3). Therefore, any EOS with TOV mass below this can be ruled out. It should be noted that rotation of the neutron star, either differential or rigid, will increase the maximum possible mass due to centrifugal support against gravitational collapse, as noted in section 3.1.

3.4.1 Other binary neutron stars parameters

Table 3 and 4 show values for various parameters for the EOS used in this project:

Waveform	$M_{TOV}(M_\odot)$	$M_{total}(M_\odot)$	$R_{TOV}(\text{km})$	$\bar{R}(\text{km})$	$M_1(M_\odot)$	$M_2(M_\odot)$	$\bar{M}(M_\odot)$	q	κ_2^T
ALF2-q10-M1225	1.9911	2.45	11.3080	12.252	1.225	1.225	1.225	1.00000	236.98
ALF2-q10-M1250	1.9911	2.50	11.3080	12.276	1.250	1.250	1.250	1.00000	212.38
ALF2-q10-M1275	1.9911	2.55	11.3080	12.298	1.275	1.275	1.275	1.00000	190.45
ALF2-q10-M1300	1.9911	2.60	11.3080	12.319	1.300	1.300	1.300	1.00000	170.81
ALF2-q10-M1325	1.9911	2.65	11.3080	12.337	1.325	1.325	1.325	1.00000	153.27
APR4-q10-M1275	2.2000	2.55	9.8733	11.060	1.275	1.275	1.275	1.00000	85.37
APR4-q10-M1300	2.2000	2.60	9.8733	11.067	1.300	1.300	1.300	1.00000	75.98
APR4-q10-M1325	2.2000	2.65	9.8733	11.073	1.325	1.325	1.325	1.00000	67.68
APR4-q10-M1350	2.2000	2.70	9.8733	11.079	1.350	1.350	1.350	1.00000	60.33
APR4-q10-M1375	2.2000	2.75	9.8733	11.084	1.375	1.375	1.375	1.00000	53.82
GAM2-q10-M1350	1.8206	2.70	12.5360	16.774	1.350	1.350	1.350	1.00000	516.73
GAM2-q10-M1375	1.8206	2.75	12.5360	16.664	1.375	1.375	1.375	1.00000	442.87
GAM2-q10-M1400	1.8206	2.80	12.5360	16.550	1.400	1.400	1.400	1.00000	379.28
GAM2-q10-M1425	1.8206	2.85	12.5360	16.434	1.425	1.425	1.425	1.00000	324.69
GAM2-q10-M1450	1.8206	2.90	12.5360	16.313	1.450	1.450	1.450	1.00000	277.51
GNH3-q09-M1300	1.9768	2.60	11.2660	13.797	1.250	1.350	1.300	0.92593	-
GNH3-q10-M1250	1.9768	2.50	11.2660	13.817	1.250	1.250	1.250	1.00000	345.42
GNH3-q10-M1275	1.9768	2.55	11.2660	13.810	1.275	1.275	1.275	1.00000	306.18
GNH3-q10-M1300	1.9768	2.60	11.2660	13.801	1.300	1.300	1.300	1.00000	271.55
GNH3-q10-M1325	1.9768	2.65	11.2660	13.790	1.325	1.325	1.325	1.00000	240.88
GNH3-q10-M1350	1.9768	2.70	11.2660	13.777	1.350	1.350	1.350	1.00000	213.77
H4-q10-M1250	2.0282	2.50	11.6030	13.533	1.250	1.250	1.250	1.00000	327.50
H4-q10-M1275	2.0282	2.55	11.6030	13.539	1.275	1.275	1.275	1.00000	292.20
H4-q10-M1300	2.0282	2.60	11.6030	13.544	1.300	1.300	1.300	1.00000	260.85
H4-q10-M1325	2.0282	2.65	11.6030	13.548	1.325	1.325	1.325	1.00000	233.11
H4-q10-M1350	2.0282	2.70	11.6030	13.550	1.350	1.350	1.350	1.00000	208.33
SLy-q09-M1300	2.0606	2.60	9.9349	11.467	1.250	1.350	1.300	0.92593	-
SLy-q10-M1250	2.0606	2.50	9.9349	11.469	1.250	1.250	1.250	1.00000	118.92
SLy-q10-M1275	2.0606	2.55	9.9349	11.470	1.275	1.275	1.275	1.00000	105.21
SLy-q10-M1300	2.0606	2.60	9.9349	11.469	1.300	1.300	1.300	1.00000	93.14
SLy-q10-M1325	2.0606	2.65	9.9349	11.468	1.325	1.325	1.325	1.00000	82.53
SLy-q10-M1350	2.0606	2.70	9.9349	11.465	1.350	1.350	1.350	1.00000	73.17

Table 3: List of neutron star parameters for the numerical relativity waveforms. M_{TOV} is the maximum non-rotating neutron star mass in M_\odot , M_{total} is the total mass of both neutron stars in M_\odot , R_{TOV} is the radius of a non-rotating neutron star at maximum mass, \bar{R} is the mean radius of the neutron star in km, M_1 and M_2 are the masses of the constituent neutron stars in M_\odot , \bar{M} is the mean mass of both neutron stars, q is the mass ratio of M_1/M_2 , κ_2^T is the total $l = 2$ coupling constant. All of these values with the exception of κ_2^T were obtained from Takami et al. (2015). κ_2^T was calculated from equation 15 for equal mass systems.

Waveform	C	$J(M_\odot^2)$	$M_{ADM}(M_\odot)$	\bar{M}_b	\bar{k}_2	Mol	$\bar{\Lambda}$	fcont(Hz)	forb(Hz)	fpeak-j(Hz)
ALF2-q10-M1225	0.14762	6.1923	2.4288	1.3373	0.132900	16.975	1263.80	1496.20	271.00	2436.46
ALF2-q10-M1250	0.15034	6.4014	2.4779	1.3672	0.130490	16.455	1132.60	1507.00	273.16	2436.46
ALF2-q10-M1275	0.15307	6.6103	2.5271	1.3971	0.128030	15.957	1015.60	1517.90	275.12	2558.28
ALF2-q10-M1300	0.15582	6.8274	2.5763	1.4272	0.125520	15.480	911.00	1529.00	277.26	2598.89
ALF2-q10-M1325	0.15858	7.0475	2.6254	1.4574	0.122970	15.021	817.44	1540.10	279.36	2639.50
APR4-q10-M1275	0.17022	6.6107	2.5271	1.4090	0.097595	12.821	455.30	1779.90	275.22	3167.39
APR4-q10-M1300	0.17344	6.8245	2.5763	1.4399	0.095396	12.436	405.19	1795.50	277.24	3126.79
APR4-q10-M1325	0.17667	7.0437	2.6254	1.4709	0.093194	12.070	360.93	1811.10	279.31	3208.00
APR4-q10-M1350	0.17992	7.2665	2.6746	1.5020	0.090990	11.720	321.78	1826.70	281.37	3248.61
APR4-q10-M1375	0.18317	7.4924	2.7237	1.5334	0.088786	11.387	287.10	1842.30	283.39	3208.00
GAM2-q10-M1350	0.11883	7.3039	2.6748	1.4336	0.097945	21.158	2755.30	980.58	282.47	2192.81
GAM2-q10-M1375	0.12183	7.5274	2.7239	1.4623	0.095091	20.203	2361.60	999.43	284.37	1908.56
GAM2-q10-M1400	0.12490	7.7540	2.7730	1.4911	0.092229	19.296	2023.00	1018.80	286.25	1989.77
GAM2-q10-M1425	0.12803	7.9838	2.8221	1.5200	0.089356	18.434	1731.50	1038.90	288.10	2030.38
GAM2-q10-M1450	0.13125	8.2167	2.8712	1.5491	0.086470	17.612	1480.30	1059.70	289.93	2030.38
GNH3-q09-M1300	0.13912	6.8255	2.5763	1.4052	0.112970	17.607	1445.20	1289.90	277.51	2395.85
GNH3-q10-M1250	0.13358	6.4067	2.4780	1.3464	0.117530	18.890	1842.40	1262.10	273.29	2314.63
GNH3-q10-M1275	0.13632	6.6187	2.5271	1.3756	0.115310	18.237	1633.00	1275.70	275.38	2314.63
GNH3-q10-M1300	0.13908	6.8340	2.5763	1.4050	0.113050	17.614	1448.10	1289.40	277.44	2436.46
GNH3-q10-M1325	0.14187	7.0538	2.6255	1.4345	0.110750	17.019	1284.70	1303.20	279.53	2436.46
GNH3-q10-M1350	0.14468	7.2766	2.6746	1.4641	0.108410	16.450	1139.90	1317.30	281.58	2517.67
H4-q10-M1250	0.13638	6.4058	2.4780	1.3506	0.123610	18.610	1746.50	1302.10	273.25	2233.42
H4-q10-M1275	0.13904	6.6191	2.5271	1.3799	0.121470	18.004	1558.30	1314.10	275.40	2355.24
H4-q10-M1300	0.14172	6.8356	2.5763	1.4094	0.119300	17.426	1391.40	1326.10	277.52	2355.24
H4-q10-M1325	0.14440	7.0552	2.6255	1.4390	0.117080	16.873	1243.10	1338.30	279.60	2477.07
H4-q10-M1350	0.14711	7.2770	2.6746	1.4687	0.114830	16.344	1111.10	1350.60	281.61	2477.07
SLY-q09-M1300	0.16739	6.8154	2.5763	1.4333	0.097828	13.115	496.28	1702.30	277.23	3126.79
SLY-q10-M1250	0.16092	6.3977	2.4779	1.3720	0.102660	14.000	634.27	1668.80	273.04	3004.96
SLY-q10-M1275	0.16413	6.6110	2.5271	1.4024	0.100250	13.545	561.11	1685.30	275.20	3248.61
SLY-q10-M1300	0.16736	6.8275	2.5763	1.4330	0.097835	13.113	496.81	1701.90	277.34	3208.00
SLY-q10-M1325	0.17060	7.0455	2.6254	1.4637	0.095415	12.702	440.20	1718.50	279.36	3208.00
SLY-q10-M1350	0.17386	7.2663	2.6745	1.4946	0.092993	12.309	390.29	1735.20	281.34	3289.22

Table 4: List of neutron star parameters for the numerical relativity waveforms. C is the compactness, J is the total angular momentum at the initial separation, M_{ADM} is the Arnowitt, Deser and Misner mass, \bar{M}_b is the mean baryonic mass, \bar{k}_2 is the dimensionless mean $l = 2$ tidal Love number, Mol is the dimensionless moment of inertial at infinite separation, $\bar{\Lambda}$ is the dimensionless tidal deformability, f_{cont} , is the contact frequency, and f_{peak-j} is frequency of maximum post- merger Fourier spectrum, f_{orb} is the orbital frequency at initial separation.

The $M_{TOV}(M_\odot)$ is the maximum non-rotating mass of a neutron star for a given EOS and R_{TOV} is the corresponding radius (in km). $M_{ADM}(M_\odot)$ is the Arnowitt, Deser and Misner mass (Arnowitt et al., 1959), $\bar{M}(M_\odot)$ is the mean mass of both neutron stars and $\bar{R}(\text{km})$ is the mean radius of both neutron stars.

$C(M_\odot/\text{km})$ is the compactness of the neutron stars defined as $C = \bar{M}/\bar{R}$, $J(M_\odot^2)$ is the total angular momentum at the initial separation of the neutron stars. M_1 and M_2 are the masses of each neutron star respectively, measured in M_\odot .

q is the mass ratio of the two neutron stars and is defined as $q = M_1/M_2$. M_b is the baryonic mass in M_\odot and \bar{k}_2 is the mean $l = 2$ dimensionless tidal Love number. The dimensionless moment of inertia at infinite separation is designated as MoI and is defined by $MoI = \bar{I}/\bar{M}^3$.

The frequency corresponding to maximum amplitude of the post-merger spectrum is defined as f_{peak-j} . f_{orb} is the orbital frequency at initial separation, and f_{cont} is the contact frequency. All frequencies are measured in Hz.

Finally there are two tidal equations that should be highlighted, $\bar{\Lambda}$ and κ_2^T . κ_2^T is the tidal

coupling constant and is defined as equation 15 (Bernuzzi et al., 2015) for equal mass BNS.

$$\kappa_2^T = \frac{\bar{k}_2}{8C^5} \quad (15)$$

The dimensionless quadrupole tidal deformability, $\bar{\Lambda}$ is defined as (Read et al., 2013):

$$\bar{\Lambda} = \frac{2\bar{k}_2}{3C^5} \quad (16)$$

4 Numerical general relativity

Takami et al. (2015) used numerical simulations of BNS mergers to examine how the EOS influenced the simulated gravitational-wave strain and the corresponding spectral response. The authors used a set of piecewise polytropes to specify the EOS from values determined from Read et al. (2009) and defined in table 2. The EOS used were GNH3, H4, ALF2, SLy and APR4. The EOS were selected due for compatibility with the maximum masses determined from J1614-2230 and J0348+0432 (see section 3.3).

These same EOS were used in Rezzolla & Takami (2016) where the inspiral, merger and post-merger signals were examined. It is worth noting that these EOS use a hybrid EOS system, incorporating a fluid that implements shock heating added to a cold EOS. The shock heating is regulated by the thermal quantity, Γ_{th} , which has been set to a value of 2, after analysis in Takami et al. (2015). This paper also notes that the Γ_{th} value directly changes the HMNS survival time due to thermal regulation.

The gravitational-wave strain was determined from the dominant spherical harmonic of $lm = 2, 2$ with a spin-weight of -2 (Rezzolla & Takami, 2016):

$$h_{+, \times} \approx [h_{+, \times}^{22}] [-_2Y_{22}(\theta, \varphi)]. \quad (17)$$

The alignment point between different simulations was determined by finding the first maximum of the strain amplitude $|h|$, where $|h|$ is defined as (Rezzolla & Takami, 2016):

$$|h| \equiv \sqrt{h_+^2 + h_\times^2}. \quad (18)$$

This point is defined as $t = 0$ and represents the time of merger in these works which is also the case for our research.

Furthermore, the following frequency domain properties of the signal need defining: the amplitude spectral density (ASD), the Fourier transform of the strain components, and the signal to noise ratio. These are defined as follows (Rezzolla & Takami, 2016):

$$\tilde{h}(f) = \sqrt{\frac{|\tilde{h}_+(f)|^2 + |\tilde{h}_\times(f)|^2}{2}}, \quad (19)$$

$$\tilde{h}_{+, \times}(f) \equiv \begin{cases} \int_0^\infty h_{+, \times}(t) e^{-i2\pi ft} dt, & (f \geq 0) \\ 0 & (f < 0), \end{cases} \quad (20)$$

$$SNR \equiv 2\sqrt{\int_0^\infty \frac{|\tilde{h}(f)|^2}{S_h(f)} df}, \quad (21)$$

where the noise PSD of the GW detector is $S_h(f)$ in units of [strain]²/Hz and as strain is dimensionless, this is usually labelled as Hz⁻¹. With these definitions made, simulations can be run and compared to the detection capabilities of LIGO (figure 5). Furthermore, specific signals can be located in the gravitational-wave strain by applying matched filter algorithms to signal templates (eg Owen & Sathyaprakash (1999)):

$$SNR \equiv \frac{\langle h, u \rangle}{\sqrt{\langle u, u \rangle}}, \quad (22)$$

where the inner product is defined as (eg Owen & Sathyaprakash (1999)):

$$\langle a, b \rangle \equiv 4\text{Re} \left[\int_0^\infty df \frac{\tilde{a}^*(f) \tilde{b}(f)}{S_h(f)} \right], \quad (23)$$

where h is the detected GW strain and u is the signal template. By setting the template and the signal under test to the same waveform, h , equation 22 becomes:

$$\rho_{opt} = \sqrt{\langle h, h \rangle} \quad (24)$$

which is known as the optimal signal to noise ratio and is numerically equivalent to equation 21.

4.1 Template requirements

Equation 22 can be used in conjunction with numerical relativity simulations to discriminate the neutron star EOS against observational data, as a different template could be generated for each EOS. The template of best match would generate the largest SNR value. To be able to detect a BNS post-merger signal, it is necessary to have $\sim 10^5 - 10^6$ template waveforms. It takes around 100,000 CPU hours to generate each waveform using full numerical relativity (Takami et al., 2015). This excludes numerical relativity as a method for generating the full set of template waveforms. This also leads into the purpose of this project, working towards a situation where we can use machine learning to generate a set of $\sim 10^5 - 10^6$ template waveforms by using numerical relativity as initial data.

4.2 Supplied data

An example of simulation output is shown in figure 8 (Rezzolla & Takami, 2016) for the five EOS listed in table 2. These are simulations of GW strain signals for HMNS of total masses starting from $2.4M_\odot$ (for $\bar{M} = 1.2M_\odot$) up to $2.7M_\odot$ (for $\bar{M} = 1.35M_\odot$).

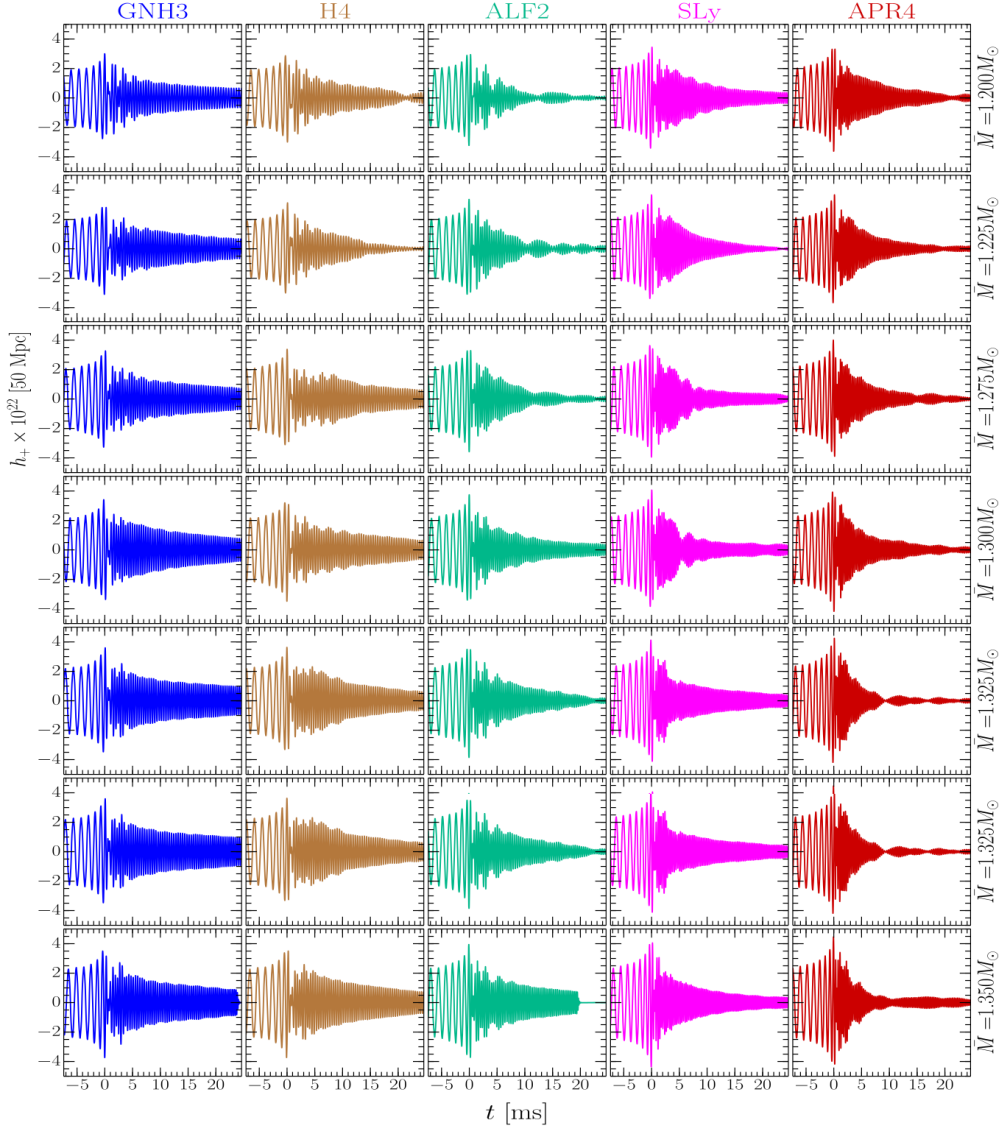


Figure 8: Plot of the simulated output for the plus polarisation of the gravitational strain versus time from Rezzolla & Takami (2016). The signals have been scaled to a distance of 50Mpc. The values in the vertical axis are unitless and the horizontal axis variable is time. There is one column for each EOS used and each EOS is colour coded. Each row of the plot represents one mass value, listed in units of M_\odot . The two neutron stars are of equal mass so that the total mass of the remnant is actually twice the value listed, assuming that there is no mass loss.

Significant differences can be seen across the timebased waveforms by comparing different mass values and different EOS. For example the response of ALF2 at $1.35M_\odot$ shows an abrupt cut-off at 20ms, most likely corresponding to sudden gravitational collapse, the same outcome is not seen with a different EOS SLY and same mass $1.35M_\odot$. Neither is it seen with the same EOS ALF2 at a different mass $1.325M_\odot$. However, the Fourier spectra provide a clearer picture to allow this discrimination. The Fourier spectra of the signals in figure 8 are shown in figure 9 (Rezzolla & Takami, 2016):

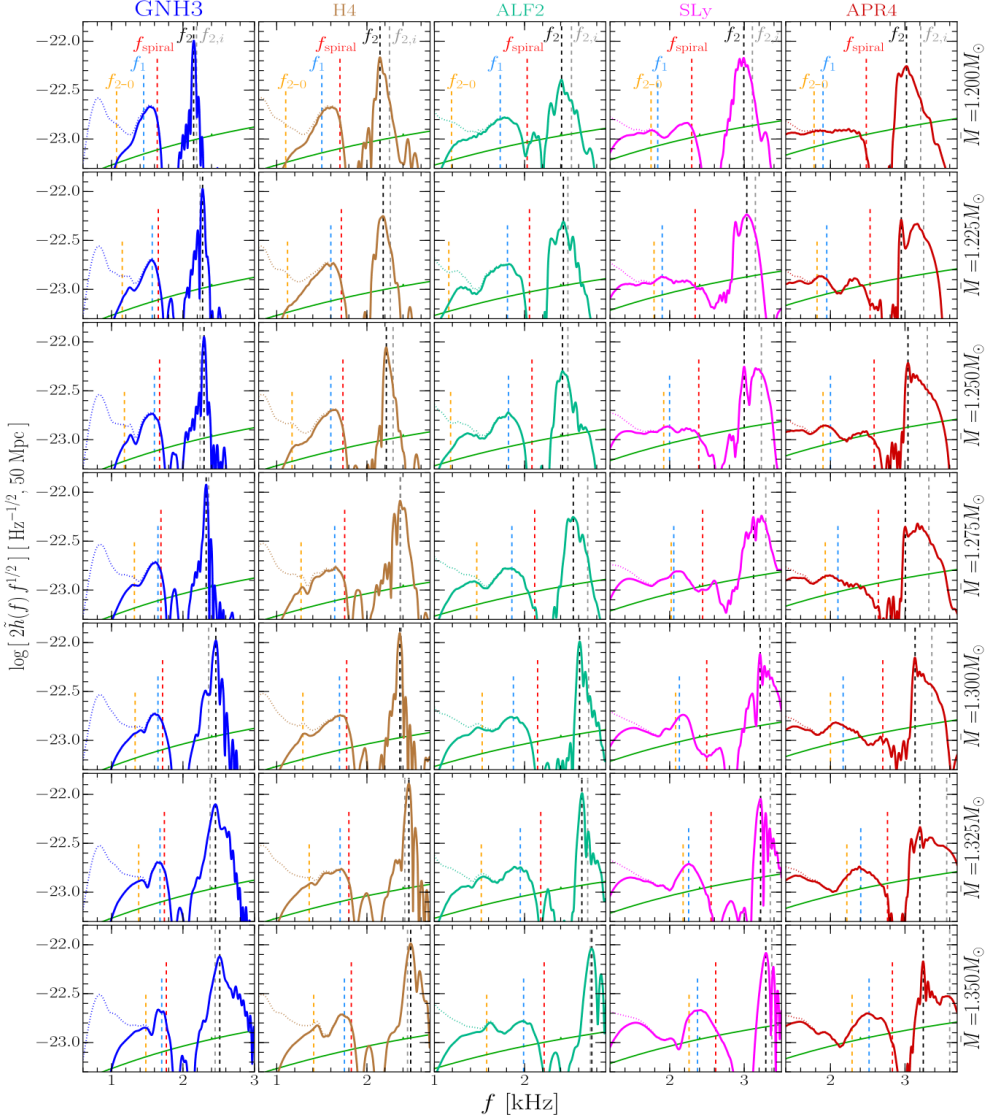


Figure 9: Amplitude spectral density corresponding to the simulated output in figure 8 from Rezzolla & Takami (2016). The signals have been scaled to a distance of 50Mpc and the detection curve for advanced LIGO at design sensitivity is shown as the angled green curve on each plot. The vertical axis is the log of the amplitude spectral density, whereas the horizontal axis variable is the frequency in kHz. There is one column for each EOS used and each EOS is colour coded. Each row of the plot represents one mass value, listed in units of M_{\odot} . The two neutron stars are of equal mass so that the total mass of the remnant is actually twice the value listed, assuming that there is no mass loss. The solid colour plots show the post-merger spectral response, whereas the dotted colour plots show the inspiral spectral response.

As suspected, variations in the frequency response are more pronounced than time response variations. For example comparing the PSD of $\bar{M} = 1.200M_{\odot}$ for EOS GNH3 (top left) and APR4 (top right) of figure 9. The higher frequency peak for GNH3 is narrow with a large peak amplitude, consistent with a long lived sinusoidal waveform, whereas the high frequency peak for APR4 is significantly wider with a smaller amplitude. Differences exist at the low frequency part of the waveforms with GNH3 exhibiting a self contained peak whereas the frequency response of APR4 extends beyond the lowest shown frequency in this spectrum. Although some features are not apparent in the frequency domain, for example, it is difficult

to visually distinguish the gravitational collapse of ALF2, $1.35M_{\odot}$ from the adjacent spectra, though, even so, it is important to note that no information is lost when performing the Fourier transform. Furthermore, it is necessary to examine signals in the frequency domain as the noise spectrum, $S_h(f)$, is required to generate signal to noise values of the gravitational-wave strain.

5 Machine learning

The machine learning can be subdivided into supervised or unsupervised problems, in addition to categorical or regression problems. Categorical problems result in discrete outcomes, for example selection from $\{\text{true}, \text{false}\}$ or $\{1, 2, 3, 4, 5\}$. If we were using a machine learning algorithm to choose an EOS from a list of choices, then this would be a categorical process. Regression problems have results that are continuous, for example determining the value of the Fourier spectrum at a given frequency or calculating the closing price for a stock on a given day. An example of a supervised machine learning process is shown in figure 10.

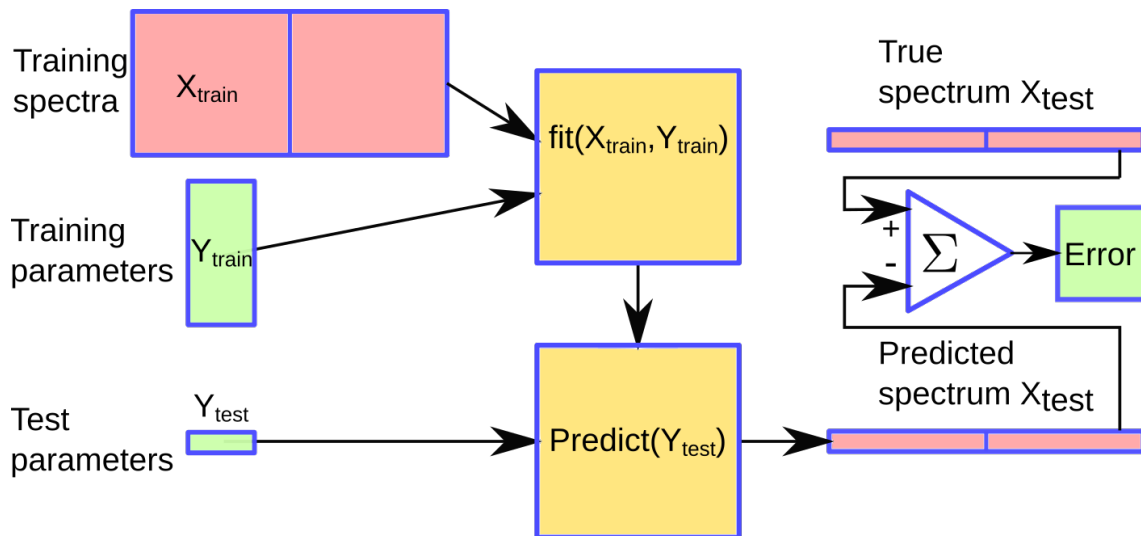


Figure 10: Block diagram of a supervised learning algorithm for predicting spectra. Training parameters and training spectra are passed into a learning command (fit in Scikit Learn) and a fit() model is generated based on the type of machine learning used. Test parameters can then be passed to a predict() command where a predicted spectra can be generated. A comparison metric can be generated by using test parameters that coincide with a known spectrum and comparing the known spectrum to the predicted spectrum.

The training inputs (the training parameters on figure 10) and outputs (the training spectra in figure 10) are analysed together by the machine learning algorithm to determine a relationship between the two sets of data. This allows the learning algorithm to predict outputs (predicted spectrum in figure 10) from new inputs (test parameters in figure 10). Furthermore, if the new input has a known output, then this can be directly compared with the predicted output to determine how successful supervised learning has been.

Unsupervised learning takes the training data and transforms it in some way, without any comparison to any input parameters. Principal component analysis (PCA) is an example of unsupervised learning algorithm, in this application the PCA algorithm takes the Fourier spectrum and encodes each spectra onto a point in PCA space (see section 5.4 for details)

5.1 Over fitting

Over fitting of a machine learning algorithm can be an issue that results from a predicted model that matches the test set too well. This is an issue because most test data has noise variations in the signals and the learning algorithm has learnt these unwanted noise signals, resulting in faulty predictions when new test data is applied.

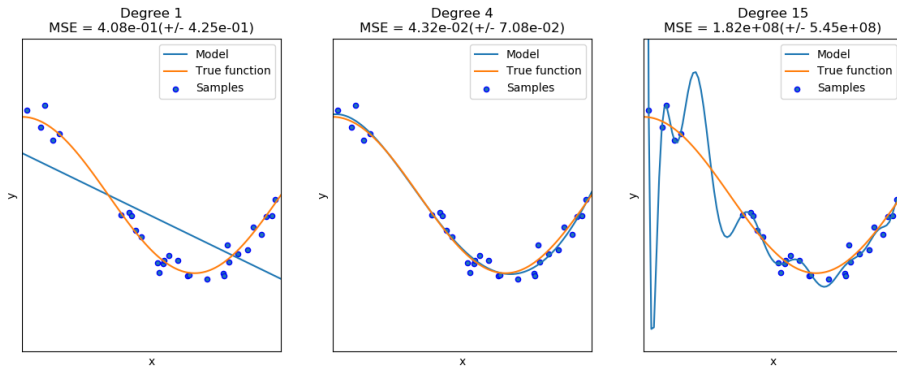


Figure 11: Plot indicating underfitting, good fitting, and overfitting. The left plot is an example of an underfit, the degrees of freedom are not sufficient to capture the shape of the data. The middle plot shows a good fit where the correct number of degrees of freedom has been selected. The right hand plot has too many degrees of freedom, and is therefore overfitted. Note that the overfit waveform passes correctly through the sample data and knowledge of the true function is used to determine that overfitting has been applied (Pedregosa et al., 2017).

5.2 Cross-validation

Cross-validation is a process where the data under test is excluded from the training set. This is performed to properly test the ability of a particular model to predict known outcomes. Different types of cross-validation systems are used, two of these are of particular interest in this project: leave one out cross-validation (LOOCV) and holdout cross-validation. Holdout cross-validation is a simple process where a percentage of the data is allocated to the training set, and the remainder is allocated to the test set. Holdout cross-validation was not an option for this project, as we had only 25 valid waveforms.

To perform leave one out cross-validation remove one item from the training set and test on this item to predict the outcome and measure the performance, then repeat the process for the next item, until all items have been used as test objects. The performance of the model is based on the average error value for all tests. We did perform LOOCV with The Cannon 2 waveforms (section 6.2.2)

5.3 Comparison metric

Using equation 21 by comparing the original strain h_{original} to the inferred strain h_{inferred} gives:

$$\begin{aligned}\Delta &= \rho_{\text{original}} - \rho_{\text{inferred}} \\ &= \frac{\langle h_{\text{original}}, h_{\text{inferred}} \rangle}{\sqrt{\langle h_{\text{original}}, h_{\text{original}} \rangle}} - \frac{\langle h_{\text{original}}, h_{\text{inferred}} \rangle}{\sqrt{\langle h_{\text{original}}, h_{\text{original}} \rangle}} \\ &= \frac{\langle h_{\text{original}} - h_{\text{inferred}}, h_{\text{original}} \rangle}{\sqrt{\langle h_{\text{original}}, h_{\text{original}} \rangle}}\end{aligned}\tag{25}$$

Which is an indication of whether it is possible to detect the difference between the original signal and the inferred signal. An alternative metric involves looking directly at the difference between the two signals and seeing if this deviation, ε , is observable:

$$\varepsilon = h_{\text{original}} - h_{\text{inferred}}\tag{26}$$

$$\rho_\varepsilon = \frac{\langle \varepsilon, \varepsilon \rangle}{\sqrt{\langle \varepsilon, \varepsilon \rangle}} = \sqrt{\langle \varepsilon, \varepsilon \rangle}\tag{27}$$

For the purpose of this project, we decided to use equation 27 for a comparison metric which is equivalent to the optimal SNR (equation 24) of the residual signal, ε , and therefore we designate this quantity as the residual SNR henceforth.

5.3.1 Frequency dependent metrics

In some of the plots in The Cannon (section 6.2) a frequency dependent metric was used to help determine which frequency values contribute the most towards the residual SNR. To do this, equation 21 was de-constructed as follows:

$$\zeta(h, f) = \frac{\|\tilde{h}(f)\| \sqrt{f}}{A_h(f)},\tag{28}$$

where $A_h(f) = \sqrt{S_h(f)}$ is the amplitude spectral density of the advanced LIGO noise curve and $\zeta(h, f)$ is the relative importance of the signal $\tilde{h}(f)$ at frequency f . Any errors in the reconstructed signal that occur when $\zeta(h, f)$ is around one or more will contribute significantly to the residual SNR. This metric can also be used to measure complex differences in signals by calculating $\zeta(h_1 - h_2)$ as follows:

$$\zeta(\Delta h, f) = \zeta(h_1 - h_2, f) = \frac{\|\tilde{h}_1(f) - \tilde{h}_2(f)\| \sqrt{f}}{A_h(f)},\tag{29}$$

where \tilde{h}_1 and \tilde{h}_2 are the two signal to be compared. Values of $\zeta(h_1 - h_2, f)$ larger than one indicate parts of the signal where \tilde{h}_1 and \tilde{h}_2 deviate significantly, leading to a large value of the residual SNR.

5.4 Principal components analysis

Principal component analysis (PCA) is an example of an unsupervised learning algorithm, that decomposes a matrix X to an ordered set of eigenvectors v_i that form an orthonormal basis for X (eg Clark et al., 2015; Wall et al., 2003):

$$X = \sum_k \beta_k \vec{v}_k\tag{30}$$

Each eigenvector is called a principal component and the first principal component has the greatest contribution to X and subsequent principal components have equal or less contributions. The ordering of the PCA principal components can be visualised in figure 12

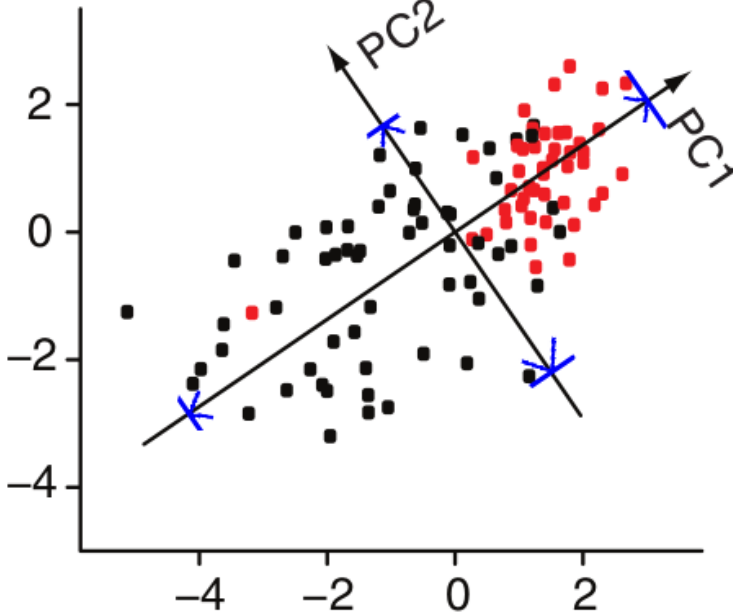


Figure 12: Schematic showing the relative importance of adjacent principal components. All principal components pass through the mean of the data, which becomes the origin in PCA space. The first principal component, designated as PC1, passes through the mean and along the path of greatest variance, the longest path through the data indicated by the blue arrows. The next principal component, PC2, moves perpendicular to PC1 along the next longest path that can be found, shown with by the smaller arrows. The path along PC2 through the data is, by construction, less than or equal to PC1. In this way the principal components are an ordered set (adapted from Ringnér, 2008).

The PCA algorithm was implemented with Scikit Learn Pedregosa et al. (2011) in python. A simplified example of the PCA code is shown here:

```
pca=PCA(num_components=3)
pca.fit(Xtrain)
PCAspace=pca.transform(Xtrain)
```

The first command determines the number of dimensions required for the PCA analysis, we used three dimensions and hence three principal components. The second line trains the PCA algorithm on the training data, and the last line determines the projections onto the three dimensional space, the β values from equation 30. Each each row of Xtrain corresponds to a spectrum for a particular EOS, mass ratio, and mean mass. For each of these rows there are three β values $\{\beta_1, \beta_2, \beta_3\}$ that position that particular spectrum in the PCA space and this is what is plotted in sections 6.1.

5.5 Preprocessing of data

The gravitation-wave strain data was read from the data supplied and redimensionalised and scaled 50Mpc distance. The data was then converted to the frequency domain using the NFFT function in the Monash GWTools package and saved as a text file for later retrieval, with one column for the time value and the other two columns for the h_+ and h_x respectively.

5.6 The Cannon 2 setup

The first machine learning algorithm that was used in this project was The Cannon 2 developed by Casey et al. (2016) which was developed to fit stellar spectra to determine information about chemical abundance and uses a modified form of L1 regularisation to predict outcomes.

5.6.1 Implementation

The Cannon 2 training method was performed on the unscaled frequency spectra from the supplied time series data with the frequency values restricted to between 10Hz and 6000Hz. The low frequency cut-off eliminated the zero frequency from the data, and the high frequency cut-off eliminated signals which were out of the detection band for LIGO. Furthermore, the spectra of the signals was quite small beyond these frequency cut-off points. The training set (X_{train} in figure 10) consisted of a matrix of all the spectra. The Cannon algorithm was trained on the following four parameters, chosen to represent major properties of the progenitor neutron stars: the mean mass \bar{M} , the compactness C , the TOV mass M_{TOV} and the tidal deformation term κ_2^T . The j -th row of the matrix Y_{train} (figure 10) consists of the parameters $\{\bar{M}, C, M_{TOV}, \kappa_2^T\}$ corresponding to the j -th EOS, mass combination. The j -th row of X_{train} consists of the spectra for the j -th EOS / mass combination. A simplified version of the Cannon 2 prediction code is shown here:

```
model=CannonModel(Ytrain , Xtrain , Variances , Parameters)
model.train()
Xprediction = model(Ytest)
CalcResidualSNR(Xtest , Xprediction)
```

This pseudo-code performs the same function as shown in figure 10. The first two lines perform the fit command, the third line performs the predictive step, and the last line calculates the residual SNR value according to equation 27.

5.7 Random forest

Random forest is a machine learning algorithm that consists of a large number of individual decision trees. Each decision tree uses a set of inputs chosen from a random subset of all available input parameters, and, from this subset, selects the input of greatest influence as the decision making input. Random forest algorithms have: good accuracy, are tolerant of noise and outliers, are faster than boosting or bagging, and are simple to implement and easy to perform in parallel Breiman (2001). The random forest algorithm can be used for both regression and classification tasks. For this project we used the random forest regressor available in Scikit Learn package Pedregosa et al. (2011) to develop our code. We chose to use frequency bin shifting to align spectral features in the real and imaginary domain of the spectrum independently. Simplified pseudo-code without cross-validation is shown here:

```
alignedXtrain=AlignSpectra(Xtrain , fpeak)
model=RandomForestRegressor()
model.fit(Ytrain , alignedXtrain)
alignedXprediction=model.predict(Ytest)
Xprediction=ReverseAlignment(alignedXprediction , ftest)
CalcResidualSNR(Xtest , Xprediction)
```

This code performs the same function as figure 10 with additional steps inserted for the frequency bin shifting. To implement cross-validation the following modified pseudocode is required:

```
alignedXtrain=AlignSpectra(Xtrain,fpeak)
model=RandomForestRegressor()
modelfreq=RandomForestRegressor()
model.fit(Ytrain, alignedXtrain)
modelfreq.fit(Ytrain, fpeak) *****
alignedXprediction=model.predict(Ytest)
fptestprediction=modelfreq.predict(Ytest) *****
Xprediction=ReverseAlignment(alignedXprediction,fptestpredict) *****
CalcResidualSNR(Xtest,Xprediction)
```

The lines marked with asterix indicate changes required to implement cross-validation. This is required because the learning algorithm does not know how to undo the initial frequency shift.

5.8 Waveform preparation

The waveforms that were used for this project were supplied by Luciano Rezzolla from Takami, Rezzolla, & Baiotti (2015). The h_{22} component of the waveform was extracted from the simulation at a distance of $500M_\odot$. The quantities supplied in these simulation data files were: time (in units of M_\odot), rh_+ , and rh_x (both in units of M_\odot). The distance from the source, d , in this project was chosen to be 50Mpc . These values were redimensionalised as:

$$t(\text{s}) = \frac{M_\odot G}{c^3} t(M_\odot) \quad (31)$$

$$\begin{aligned} h_{+,d}(M_\odot) &= \left(\frac{r}{d}\right) h_{+,r} = \frac{rh_{+,r}}{d} = \frac{rh_{+,r}(M_\odot)}{d} \\ h_{+,d}(\text{m.m}^{-1}) &= (rh_{+,r}(M_\odot)) \times \frac{M_\odot G}{50c^2 [1 \text{ Mpc}]} \approx 9.5708 \times 10^{-22} (rh_{+,r}(M_\odot)), \end{aligned} \quad (32)$$

where $h_{+,r}$ and $h_{+,d}$ are the plus polarisation of the gravitational-wave strain at respective distances of r and d from the source respectively. The gravitational strain, $h_{+,d}$, is a dimensionless term after redimensionalising. During this thesis h_+ will refer to $h_{+,d}$, the strain at distance $d = 50\text{Mpc}$ from the source. The time series data was not directly used for this project, this data was converted into the frequency domain by performing a fast Fourier transform on the time series data. As mentioned in section 4, the zero time point coincides with the time of merger and in the following sections, the time series waveforms were truncated to positive time values corresponding to the post-merger region. This simplified the coding process required for frequency scaling (see section 6.1.1) and allowed concentration of the spectral properties of the post-merger spectra. This restriction will be dropped for future investigation into this topic, as we ultimately require a system that works with both the inspiral and post-merger signals.

5.9 Numerical relativity waveforms

Tables 3 and 4 show a list of the names of the waveforms available and their corresponding parameters.

The waveforms designated as GAM2 were simple polytropes with a fixed $\Gamma = 2.0$. The spectra generated by these waveforms was qualitatively quite different to the more realistic waveforms with piecewise polytropes (see section 4 and table 2) and were therefore excluded from the waveforms under test. Furthermore, as we only had two waveforms with an unequal mass ratio, we decided to exclude these waveforms from The Cannon 2 machine learning data set, though these waveforms were still used for PCA decomposition and the random forest analysis.

6 Results

6.1 Principal components analysis

One of the papers that served as initial inspiration for this research project was Clark, Bauswein, Stergioulas, & Shoemaker (2015). Clark et al. (2015) used principal component analysis on the gravitational-wave spectra of the signals for various EOS and mass values. Principal component analysis (PCA) uses a decomposition process to order principal components from most significant to least significant, specific details are shown in section 5.4. Each principal component corresponds to one axis in PCA space, and the coefficients created from the decomposition of an individual waveform are represented by a single point in the PCA space. PCA decomposition does not give any information on what each of the principal components represent, but it can be useful for categorisation and finding relationships between different signals. We performed PCA decomposition on both scaled (section 6.1.1) and unscaled (section 6.1.2) frequency waveforms.

6.1.1 Scaled Frequency

Before performing PCA decomposition on their waveforms, Clark et al. (2015) implemented frequency scaling on their data. The new frequency values were calculated as shown in equation 33:

$$F'_j = F_j \left(\frac{f_{\text{peak}}}{f_{\text{peak-}j}} \right), \quad (33)$$

where $f_{\text{peak-}j}$ is the frequency corresponding to the peak amplitude of the FFT for waveform j . The peak frequency value, f_{peak} is a free value that can be chosen. We used the same frequency scaling as Clark et al. (2015) to generate PCA decomposition on our waveforms with three principal components. An important consideration was that the frequency values for one waveform to the next no longer matched after this transformation. Furthermore, it was necessary to have a common frequency value for each of the FFT waveforms to enable PCA analysis on the data. Because of this, the complex FFT amplitude, H_j , was interpolated onto a fixed set of frequency values which were set to be the same for all waveforms. Note also that it was necessary to reverse this transform before performing an inverse FFT to generate time series data.

The frequency range was restricted from 600 to 8000Hz, which is the frequency range of interest for the post-merger signals. The PCA decomposition was performed on both the amplitude and phase of the Fourier spectrum. Figure 13 shows the result of this decomposition for the amplitude of the Fourier spectra.

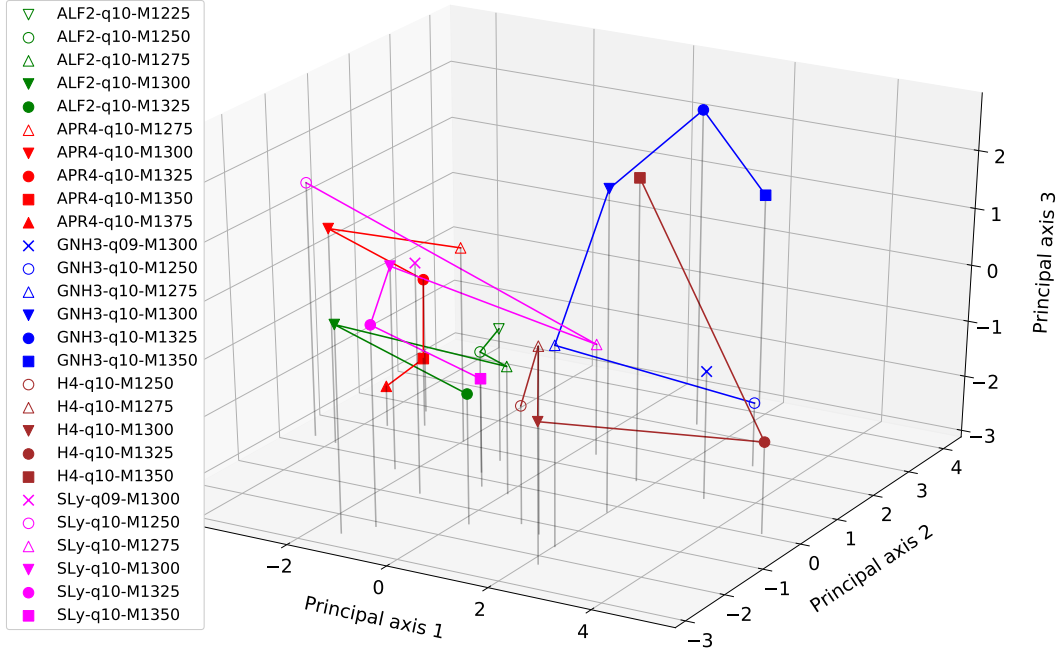


Figure 13: Three component PCA of the Fourier transform amplitude with frequency scaling. Each equation of state is designated by a different colour and each mass value a different marker. An appropriately coloured line connects adjacent mass values for a given equation of state for equal mass ratio values. The two points with non-equal mass ratio are not connected on these lines and are designated as x on the plots. Faint vertical lines are drawn to locate each point in the two dimensional space generated from principal axes 1 and 2.

Each EOS is shown in a different colour, corresponding to the same colours used in figures 8 and 9. For equal mass systems ($q = 1.0$) a line was drawn to connect adjacent mass values for the same EOS. This was to aid in determining whether any pattern or correlation could be visually seen corresponding to increasing mass, but the locus through the PCA space appears disjointed. The waveforms are designated as follows: EEEE-QQQ-MYXXX, where: 1) EEEE is the EOS used, 2) QQQ is the mass ratio, either 1.0 (q10) or 0.92593 (q09), 3) MYXXX is the mean mass value of both neutron stars with a mass of Y.XXX, so M1350 refers to a system with mean mass of $1.350M_{\odot}$. Vertical grey lines were projected downward to the X,Y plane of the principal axes 1 and 2, to aid visual placement of the markers in the three dimensional space. Projecting this information down to the XY plane aids the interpretation of this plot and is shown in figure 14.

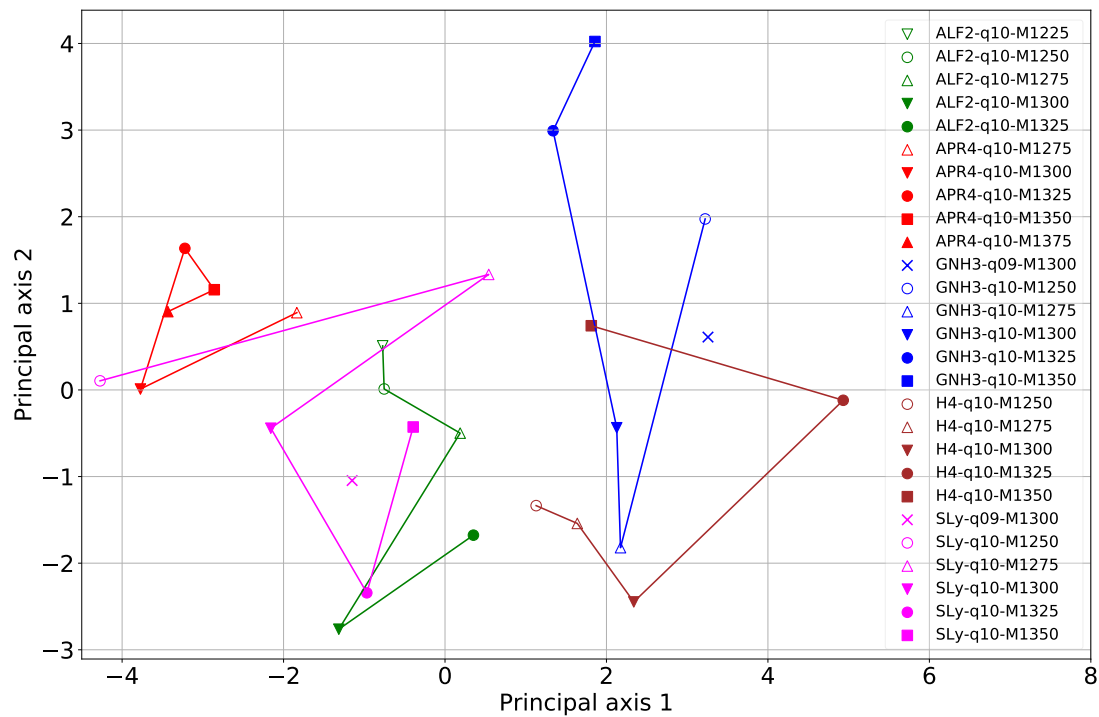


Figure 14: Three component PCA of the fourier transform amplitude projected onto two dimensions with frequency scaling applied. Each equation of state is designated by a different colour and each mass value a different marker. A line connects adjacent mass values for a given equation of state for equal mass ratio values. The two points with non-equal mass ratio are not connected on these lines and are designated as x on the plots.

The H4 and the GNH3 EOS occupy roughly the same part of the PCA space, and the other three EOSs, ALF2, APR4 and SLy, occupy another distinct part of PCA space. However, when comparing with tables 3 and 4, there is no clear parameter that allows for this distinction between these two classes of EOS. Another important consideration is that the locus through the PCA space is still quite disjointed, and difficult to find correlations by eye, but this may be such a situation where machine learning can aid in the determination of any correlations.

Figure 15 shows the corresponding phase response for the frequency scaled waveforms in three component PCA space.

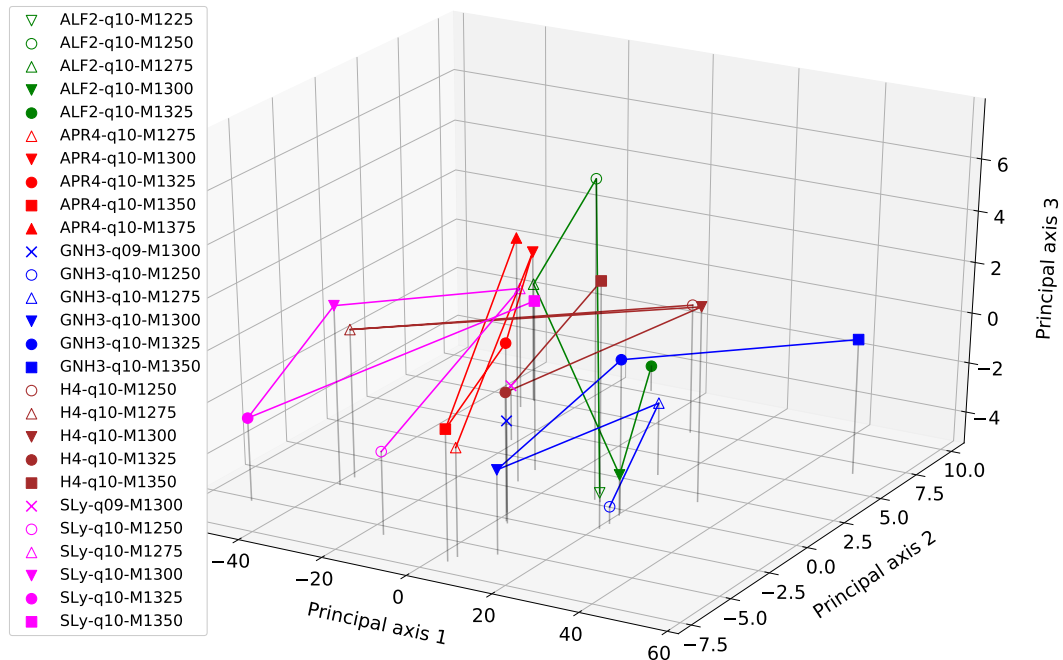


Figure 15: Three component PCA of the fourier transform phase with frequency scaling. Each equation of state is designated by a different colour and each mass value a different marker. An appropriately coloured line connects adjacent mass values for a given equation of state for equal mass ratio values. The two points with non-equal mass ratio are not connected on these lines and are designated as x on the plots. Faint vertical lines are drawn to locate each point in the two dimensional space generated from principal axes 1 and 2. There is little separation between different points in PCA space making it difficult to visually find correlations between the different EOS and mass combinations.

The distinction between different EOS in PCA phase space is even more difficult, the different points in phase space appear to exhibit significant overlap. Figure 16 shows the projection of figure 15 down to the XY plane to aid in the analysis of this data.

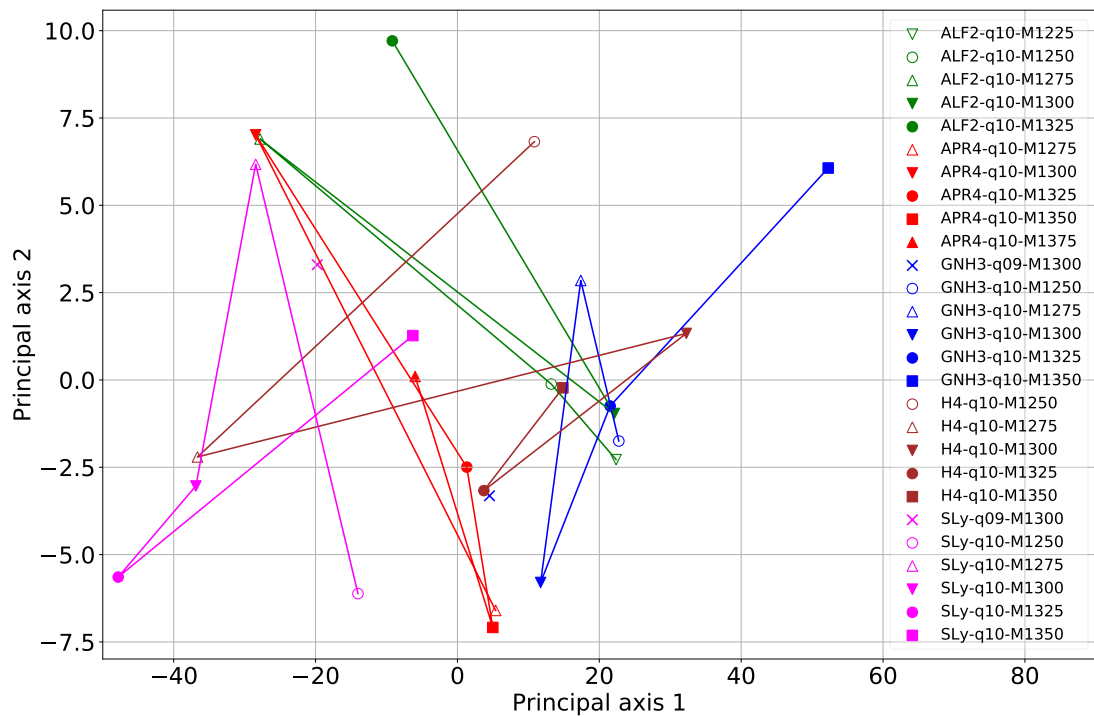


Figure 16: Three component PCA of the fourier transform phase projected onto two dimensions with frequency scaling applied. Each equation of state is designated by a different colour and each mass value a different marker. A line connects adjacent mass values for a given equation of state for equal mass ratio values. The two points with non-equal mass ratio are not connected on these lines and are designated as x on the plots.

A significant overlap is also shown in the XY projection of the PCA frequency scaled phase space, showing the difficulty in visually distinguishing between different EOS. It may be possible that the PCA decomposition without frequency scaling would be more insightful and this is investigated in the following section.

6.1.2 Unscaled Frequency

We generated a three component PCA decomposition of the unmodified Fourier transform of the waveform under test. Figure 17 shows the PCA response for the amplitude of the waveforms under test:

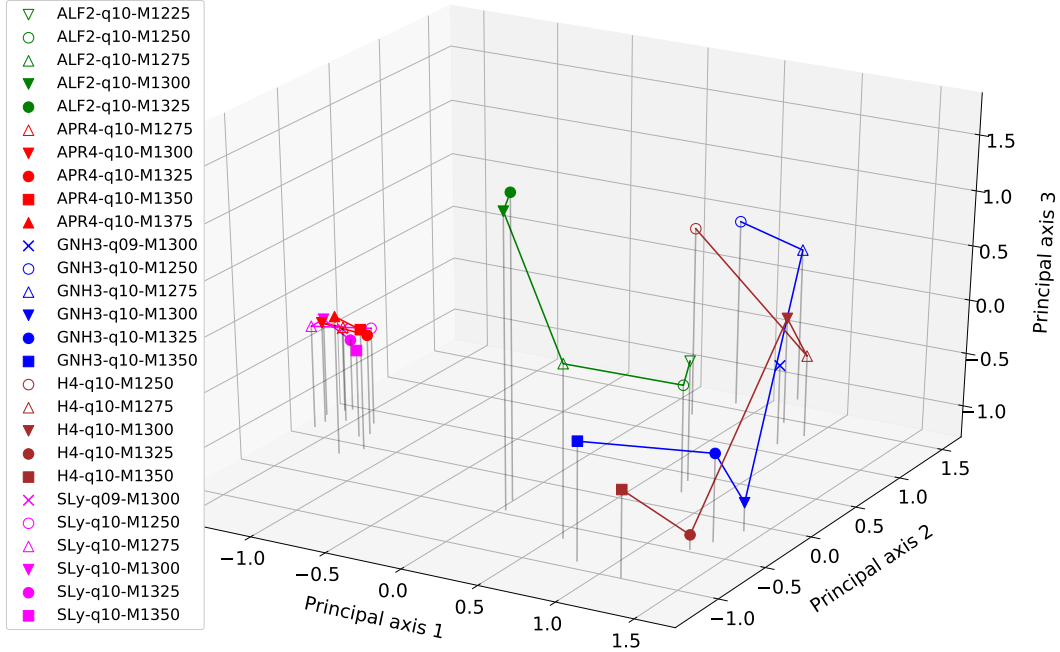


Figure 17: Three component PCA of the fourier transform amplitude with no frequency scaling. Each equation of state is designated by a different colour and each mass value a different marker. An appropriately coloured line connects adjacent mass values for a given equation of state for equal mass ratio values. The two points with non-equal mass ratio are not connected on these lines and are designated as x on the plots. Faint vertical lines are drawn to locate each point in the two dimensional space generated from principal axes 1 and 2.

Without frequency scaling, there seems to be more separation of each EOS. This seems more promising as a potential input data-set for machine learning. There is still a tight clustering of the two EOS APR4 and SLy. However, if table 4 is consulted, the strongest visual correlation between the first principal axis and peak frequency f_{peak-j} with negative x values corresponding to high peak frequencies and vice versa. This explains why this correlation is lost when frequency scaling occurs. Projecting the three dimensional PCA plot down to the XY plane presents an even clearer picture of the PCA amplitude space:

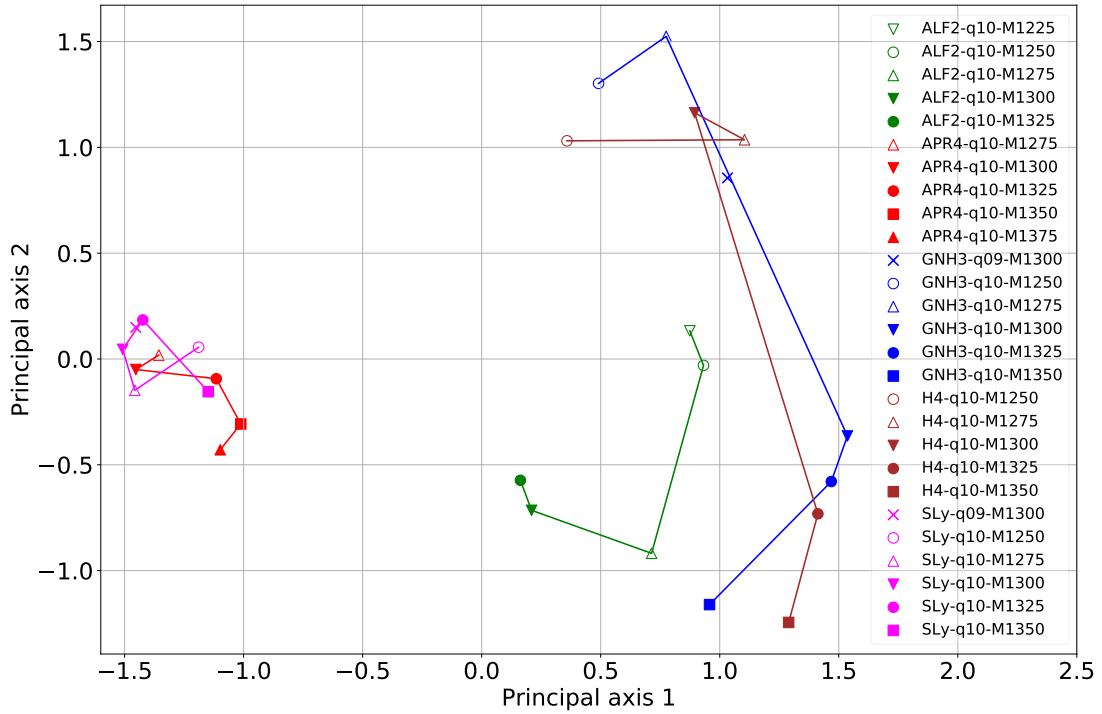


Figure 18: Three component PCA of the fourier transform amplitude projected onto two dimensions with no frequency scaling. Each equation of state is designated by a different colour and each mass value a different marker. A line connects adjacent mass values for a given equation of state for equal mass ratio values. The two points with non-equal mass ratio are not connected on these lines and are designated as x on the plots.

The large gap observed in the PCA space between the EOS APR4/SLy and ALF2/GNH3/H4 seems to correspond mainly to differences in peak frequency and to a lesser degree the compactness, and other tidal parameters. It should also be noted that Bernuzzi et al. (2015) developed a relationship between f_{peak} , the average mass (\bar{M}), and the tidal parameter (κ_2^T), indicating that it may be possible to eliminate f_{peak} as a parameter by using the tidal parameters instead. This is preferable for the unscaled frequency system, as it means that there is no pre-processing involved. Looking now at the phase response for the unscaled waveforms as shown in figure 19:

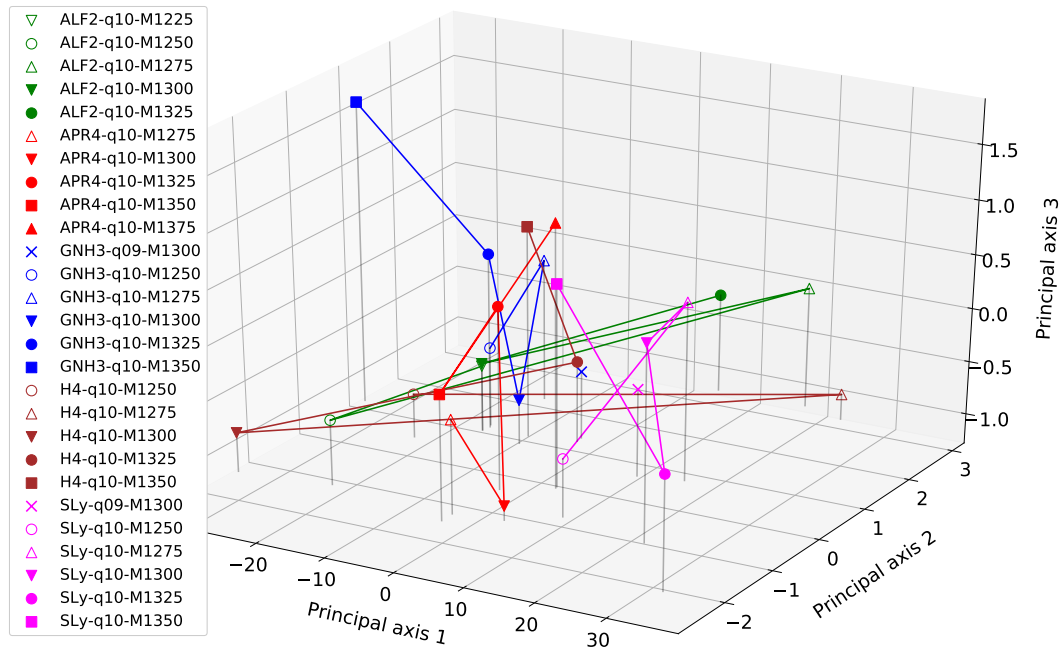


Figure 19: Three component PCA of the fourier transform phase with no frequency scaling. Each equation of state is designated by a different colour and each mass value a different marker. An appropriately coloured line connects adjacent mass values for a given equation of state for equal mass ratio values. The two points with non-equal mass ratio are not connected on these lines and are designated as x on the plots. Faint vertical lines are drawn to locate each point in the two dimensional space generated from principal axes 1 and 2.

The phase response looks quite tangled, as with the scaled response in figure 13, so projection to the XY plane was performed to give figure 20:

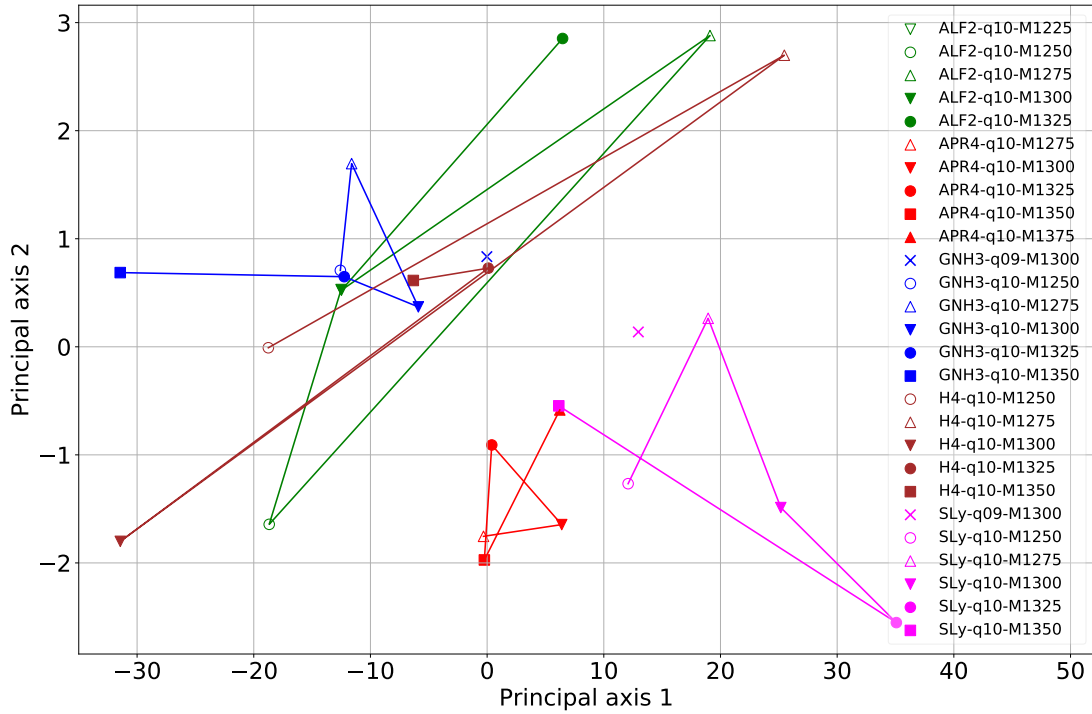


Figure 20: Three component PCA of the fourier transform phase projected onto two dimensions with no frequency scaling. Each equation of state is designated by a different colour and each mass value a different marker. A line connects adjacent mass values for a given equation of state for equal mass ratio values. The two points with non-equal mass ratio are not connected on these lines and are designated as x on the plots.

Here we can still clearly see a distinction between the APR4/SLy and ALF2/GNH3/H4 equation of states which was not visible in three dimensional PCA space suggesting that a machine learning algorithm would be better using the unscaled Fourier spectra.

6.1.3 Principal components summary

The PCA analysis on both the scaled and unscaled frequency values for the Fourier transform of the waveforms suggests that a learning algorithm may be more successful using the unscaled frequency values for the FFT of the gravitational-wave strain signals rather than the frequency scaled data. This is examined in section 6.2.

6.2 The Cannon analysis

The Cannon 2 implementation was setup as described in section 5.6 and the waveforms have been restricted to equal mass systems with the EOS GAM2 excluded. I have also selected two waveforms to use as example signals: APR4 EOS, with an average mass of $1.275M_{\odot}$, and ALF2 EOS with average mass of $1.225M_{\odot}$. There has been no frequency scaling for analysis performed using the Cannon algorithm. The following plots show the amplitude of the Fourier transform multiplied by the square root of the frequency as this value is often used in numerical relativity (eg Clark et al., 2015; Takami et al., 2015) because it can be directly compared with the LIGO amplitude spectral density.

6.2.1 Entire training set

The entire training set was used for this section and leave one out cross-validation was performed in section 6.2.2. Figure 21 shows the response generated from APR4 EOS with a mean mass of $1.275M_{\odot}$ using the Cannon algorithm.

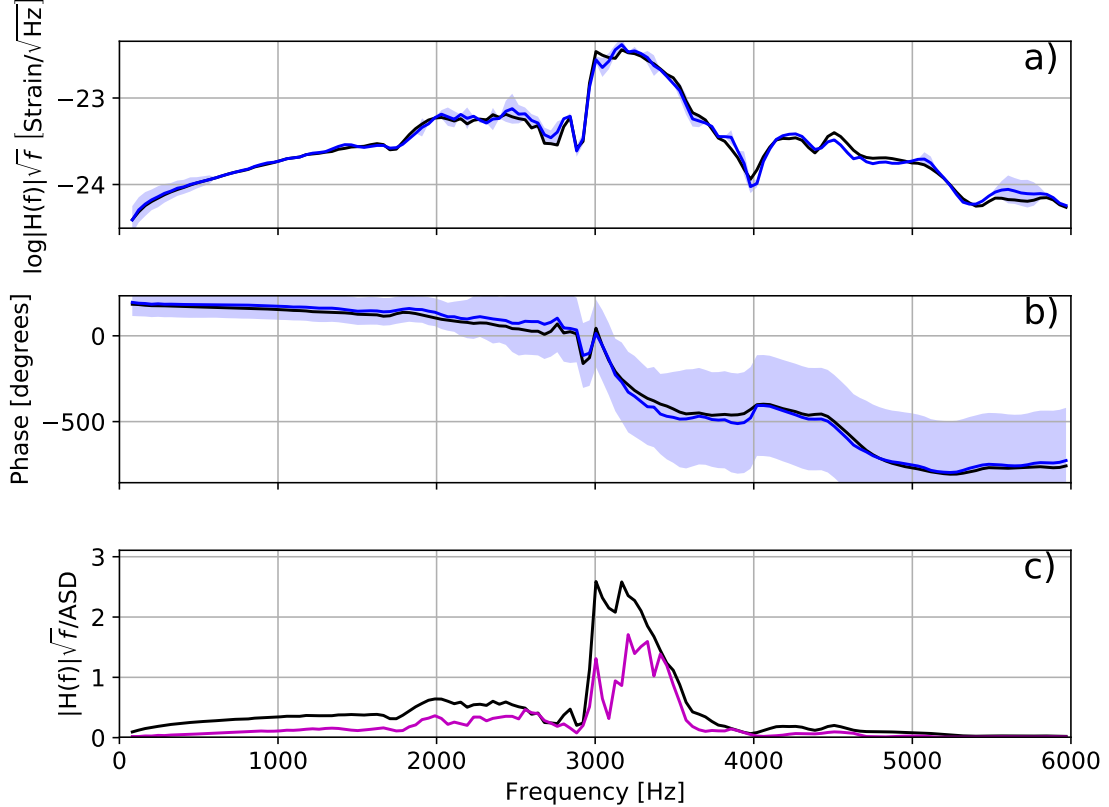


Figure 21: Frequency response of waveform APR4-q10-M1275 and corresponding error signal. The total SNR value for this signal is 2.06 and the residual SNR value is 1.10. Plot a) amplitude response multiplied by \sqrt{f} . The black trace is the original signal and the blue trace is the signal inferred from The Cannon 2. The shaded blue area represents the uncertainty in the inferred reconstruction. Plot b) phase response with the same traces as specified in plot a). Plot c) residual SNR plot, the black trace is the magnitude of the signal multiplied by \sqrt{f} and divided by the advanced LIGO amplitude spectral density noise value. Values larger than one indicates parts of the signal that significantly contribute towards the detected LIGO SNR value. The pink trace represents the magnitude of complex subtraction of the original signal and the inferred signal, again scaled by \sqrt{f} and the LIGO amplitude spectral density noise curve. Values larger than one significantly contribute to the residual SNR value.

The total SNR for this signal is 2.06 and the residual SNR was 1.10. The goal of the residual SNR plots is to achieve a number significantly less than one, this is to ensure that the reconstructed waveform is indistinguishable. Plot a) shows the amplitude response of APR4/1.275M $_{\odot}$ scaled by the square root of the frequency in log based 10 units. The black trace is the original FFT amplitude of the signal, and the blue trace is the reconstructed signal determined by the learning algorithm. Plot b) shows the phase response in degrees with black trace referring to the phase of the original FFT, and the blue trace referring to the reconstructed phase of the FFT, generated by The Cannon model. The shaded blue area in both of these plots indicate the uncertainty in the amplitude or phase of the model. Plot c)

gives an indication of the errors in the reconstructed signal, where the error in the signal is given by the complex difference between the original signal and the reconstructed signal. The black trace shows $\zeta(h, f)$, the significance of the original signal for a given frequency (equation 28). The pink trace $\zeta(\Delta h, f)$ (equation 29) shows the significance of the error in the reconstructed waveform for a given frequency. For this waveform, the error of the signal is around half the signal strength. Figure 22 shows the corresponding response of ALF2/1.225M_⊙.

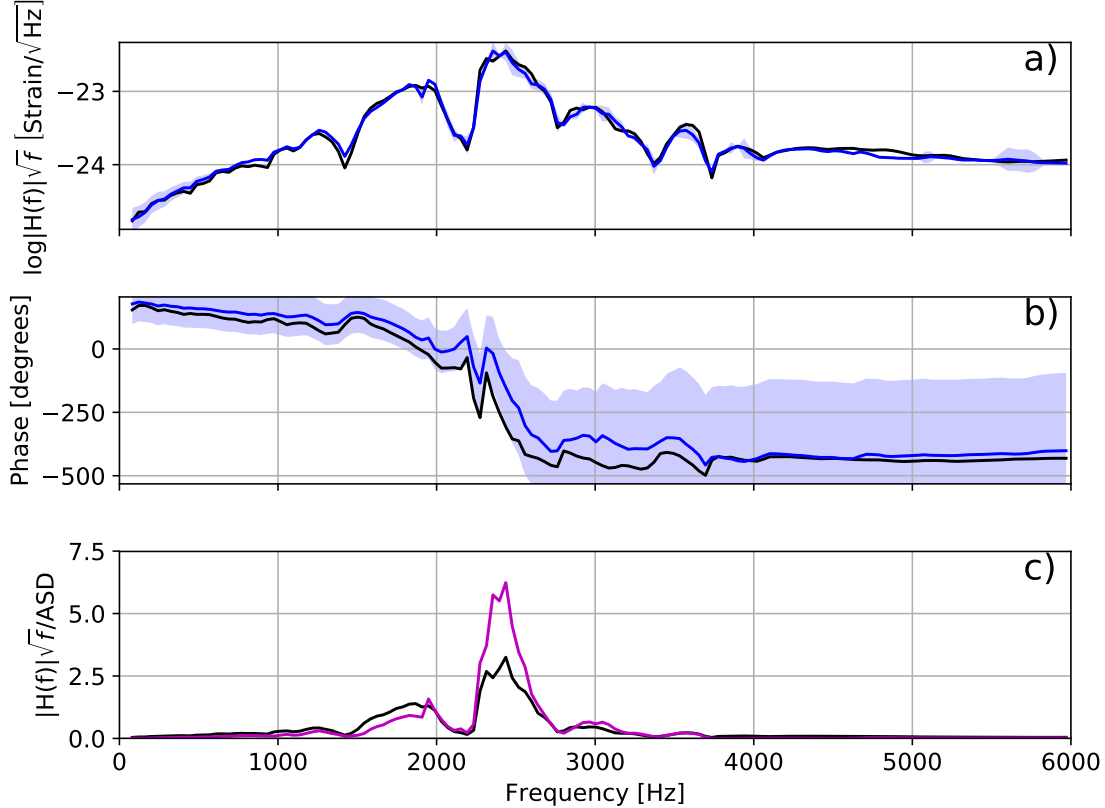


Figure 22: Frequency response of waveform ALF2-q10-M1225 and corresponding error signal. The total SNR value for this signal is 2.33 and the residual SNR value is 3.56. Plot a) amplitude response multiplied by \sqrt{f} . The black trace is the original signal and the blue trace is the signal inferred from The Cannon 2. The shaded blue area represents the uncertainty in the inferred reconstruction. Plot b) phase response with the same traces as specified in plot a). Plot c) residual SNR plot, the black trace is the magnitude of the signal multiplied by \sqrt{f} and divided by the advanced LIGO amplitude spectral density noise value. Values larger than one indicates parts of the signal that significantly contribute towards the detected LIGO SNR value. The pink trace represents the magnitude of complex subtraction of the original signal and the inferred signal, again scaled by \sqrt{f} and the LIGO amplitude spectral density noise curve. Values larger than one significantly contribute to the residual SNR value.

The SNR for this signal is 2.33 and the residual SNR was 3.56. Looking at plot c) it can be seen that the maximum error occurs around the maximum amplitude. The amplitude in plot a) looks fairly close to the original signal, however the phase is off by around 180 degrees, which is consistent with an error value of twice the original signal, as observed in the pink plot of $\zeta(\Delta h, f)$. The residual SNR for this signal is too high even though the waveform under test was included in the training set. However, cross-validation is required to get a complete picture of the performance of this method as is investigated in the following section.

6.2.2 Leave one out cross-validation

Figures 22 and 21 are not true cross-validation waveforms. Although the waveform parameters are inferred from the learning mode, the signals under test were included in the training set. To perform leave one out cross-validation (see section 5.2), the signals under test should be excluded from the training set, as performed in this section. Figure 23 shows the cross-validation waveform for APR4/1.275M_⊙:

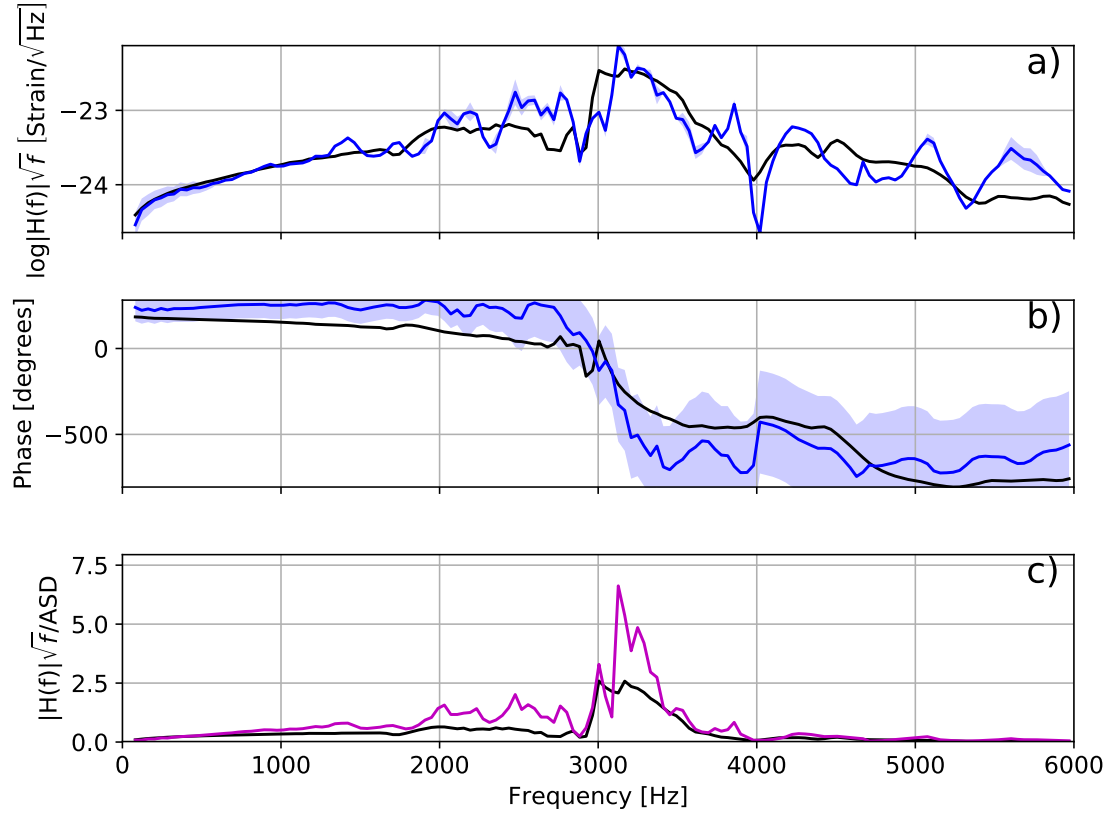


Figure 23: Leave one out cross validation frequency response of waveform APR4-q10-M1275 and corresponding error signal. The total SNR value for this signal is 2.06 and the residual SNR value is 3.63 . Plot a) amplitude response multiplied by \sqrt{f} . The black trace is the original signal and the blue trace is the signal inferred from The Cannon 2. The shaded blue area represents the uncertainty in the inferred reconstruction. Plot b) phase response with the same traces as specified in plot a). Plot c) residual SNR plot, the black trace is the magnitude of the signal multiplied by \sqrt{f} and divided by the advanced LIGO amplitude spectral density noise value. Values larger than one indicates parts of the signal that significantly contribute towards the detected LIGO SNR value. The pink trace represents the magnitude of complex subtraction of the original signal and the inferred signal, again scaled by \sqrt{f} and the LIGO amplitude spectral density noise curve. Values larger than one significantly contribute to the residual SNR value. It can be clearly seen that the leave one out cross validation produces a very poor response with this method.

The residual SNR for this waveform is now 3.63, compared to 1.10 without cross-validation (figure 21), so it is clear that leave one out cross-validation causes significant deterioration in the residual SNR. This could potentially be explained by the small quantity of waveforms within the training set. Cross-validation is often performed with 30% of the waveforms used as the test set, and the remaining 70% of the waveforms used for the training set. This is not an option when there are only 25 waveforms to start with, and clearly, even leaving one

waveform out results in poor training in this situation. The second waveform under test is shown in 24:

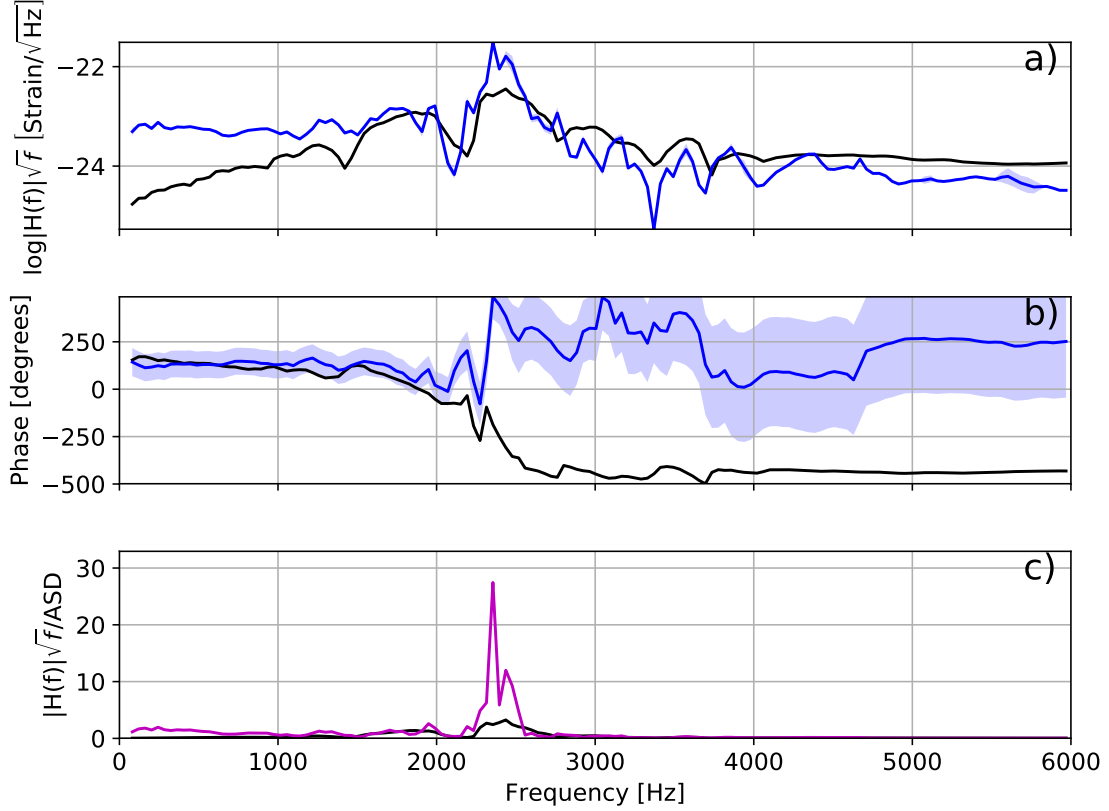


Figure 24: Leave one out cross validation frequency response of waveform ALF2-q10-M1225 and corresponding error signal. The total SNR value for this signal is 2.33 and the residual SNR value is 10.05 . Plot a) amplitude response multiplied by \sqrt{f} . The black trace is the original signal and the blue trace is the signal inferred from The Cannon 2. The shaded blue area represents the uncertainty in the inferred reconstruction. Plot b) phase response with the same traces as specified in plot a). Plot c) residual SNR plot, the black trace is the magnitude of the signal multiplied by \sqrt{f} and divided by the advanced LIGO amplitude spectral density noise value. Values larger than one indicates parts of the signal that significantly contribute towards the detected LIGO SNR value. The pink trace represents the magnitude of complex subtraction of the original signal and the inferred signal, again scaled by \sqrt{f} and the LIGO amplitude spectral density noise curve. Values larger than one significantly contribute to the residual SNR value. It can be clearly seen that the leave one out cross validation produces a very poor response with this method.

The deterioration in the residual SNR is more extreme, going from 3.56 (in figure 22) to 10.05 in this figure. The amplitude deviates significantly around the peak of the waveform, resulting in a large error term of around 28 as can be seen in the pink curve on plot c). Using a sample of two waveforms from 25 does not give the overall picture, it may be that these two waveforms are better or worse than the rest and are not a representative sample. A histogram of residual SNR was generated for all leave one out cross-validation waveforms for The Cannon and is shown in figure 25.

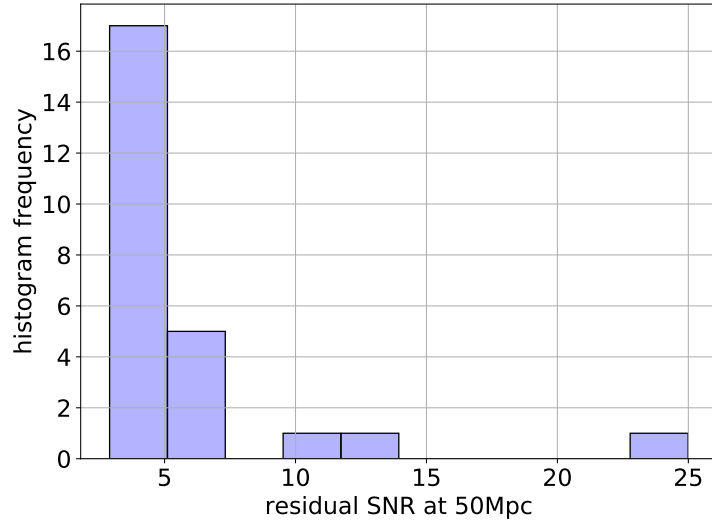


Figure 25: Histogram of the residual signal to noise ratio for leave one out cross validation of The Cannon 2 algorithm.

The residual SNR values range from around 2.0 to up to near 25, though the majority look to be less than 7.0. Furthermore, if waveforms with residual SNR above 7.0 are designated as outliers, then one of the test waveforms, ALF2/1.225M \odot falls into this category. Allowing for the removal of these outliers results in figure 26:

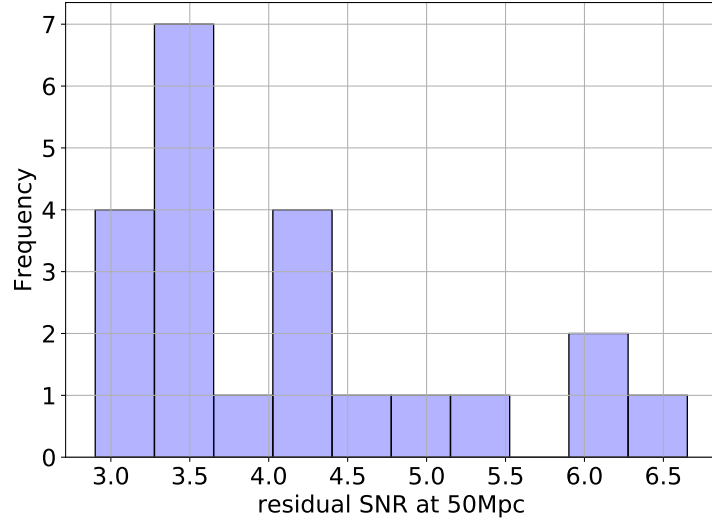


Figure 26: Histogram of the residual signal to noise ratio for leave one out cross validation of The Cannon 2 algorithm with outliers excluded.

These residual SNR values still appear much too large even when the outliers have been removed and the machine learning algorithm should work with all waveforms, not just a selection of them. Therefore we do not wish to exclude any outliers.

6.2.3 Training on real and imaginary components of the Fourier transform of the signals

It is possible that the large residual SNR values obtained in the previous section could be caused by the interaction between the learning algorithm and the wrapping of the phase. The SNR residual metric (see section 5.3) compares the signals in the complex domain, so that a signal with a phase angle of slightly less than π is similar to a signal with a phase angle of slightly larger than $-\pi$. Whereas The Cannon algorithm when supplied with phase information, considers these two signals widely apart. This could have been compensated for by adjusting the comparison metric, but time constraints prevented this modification of The Cannon 2 code. Wrapping the phase angle between $-\pi$ and π did not help very much either. This is still likely to the learning algorithm not realising the proximity of $-\pi$ and π as mentioned above. To investigate whether this was truly a factor in the poor performance of the system with complex values, the machine learning process was repeated while training on the real and imaginary parts of the Fourier spectra, rather than the amplitude and the phase of the spectra.

Figure 27 shows The Cannon response when trained on the real and imaginary parts of APR/1.275M_⊙:

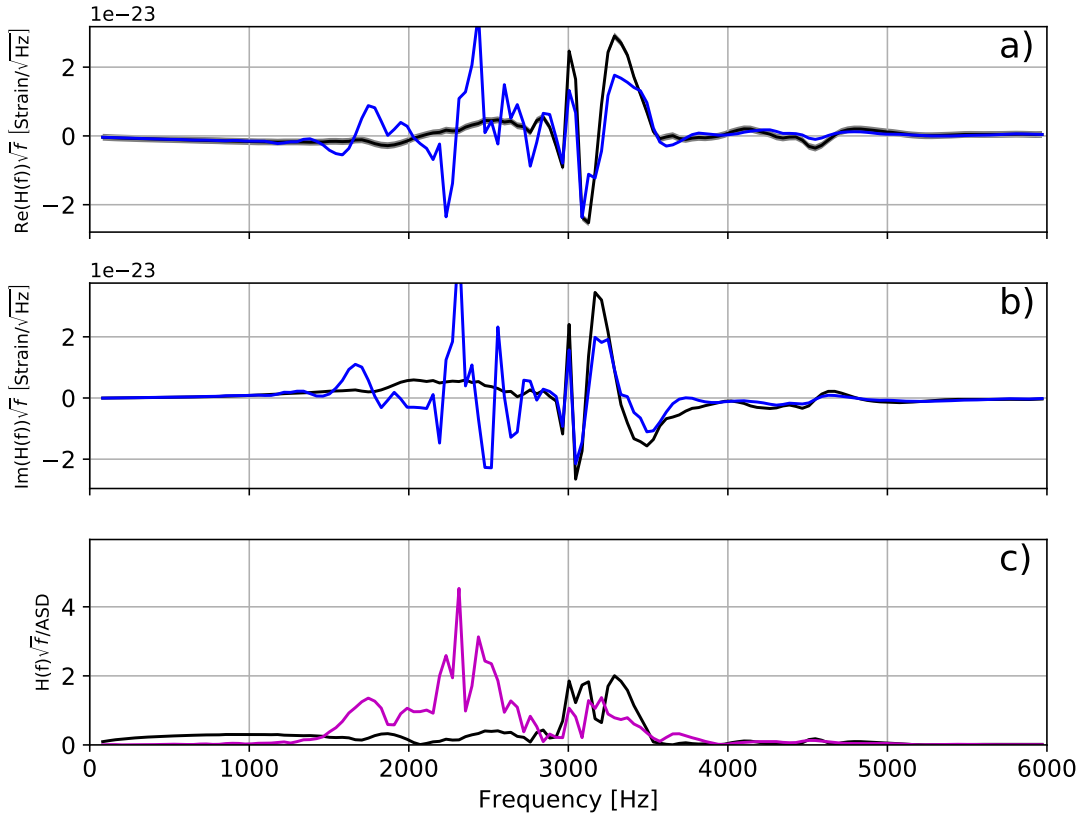


Figure 27: Complex frequency response of waveform APR4-q10-M1275 and corresponding error signal when trained on the real and imaginary parts of the Fourier response using The Cannon 2 algorithm. The total SNR value for this signal is 2.06 and the residual SNR value is 2.57. Plot a) real part of the amplitude response multiplied by \sqrt{f} . The black trace is the original signal and the blue trace is the signal inferred from The Cannon 2 training on this signal without cross validation. Plot b) imaginary part corresponding to the signals shown in plot a). Plot c) residual SNR plot, the black trace is the magnitude of the signal multiplied by \sqrt{f} and divided by the advanced LIGO amplitude spectral density noise value. Values larger than one indicates parts of the signal that significantly contribute towards the detected LIGO SNR value. The pink trace shows the magnitude of the complex subtraction between the original signal and the inferred signal, scaled by \sqrt{f} and divided by the LIGO amplitude spectral density noise curve. Values larger than one significantly contribute to the residual SNR value.

The residual SNR has increased from 1.10 (figure 21) when trained on the amplitude and phase of the FFT, to 2.57 when trained on the corresponding real and imaginary parts. The visual correlation between the original image and the inferred image is quite poor which is reflected in the error function shown on part c) of the plot. The response for ALF2/1.225M $_{\odot}$ is shown in figure 28:

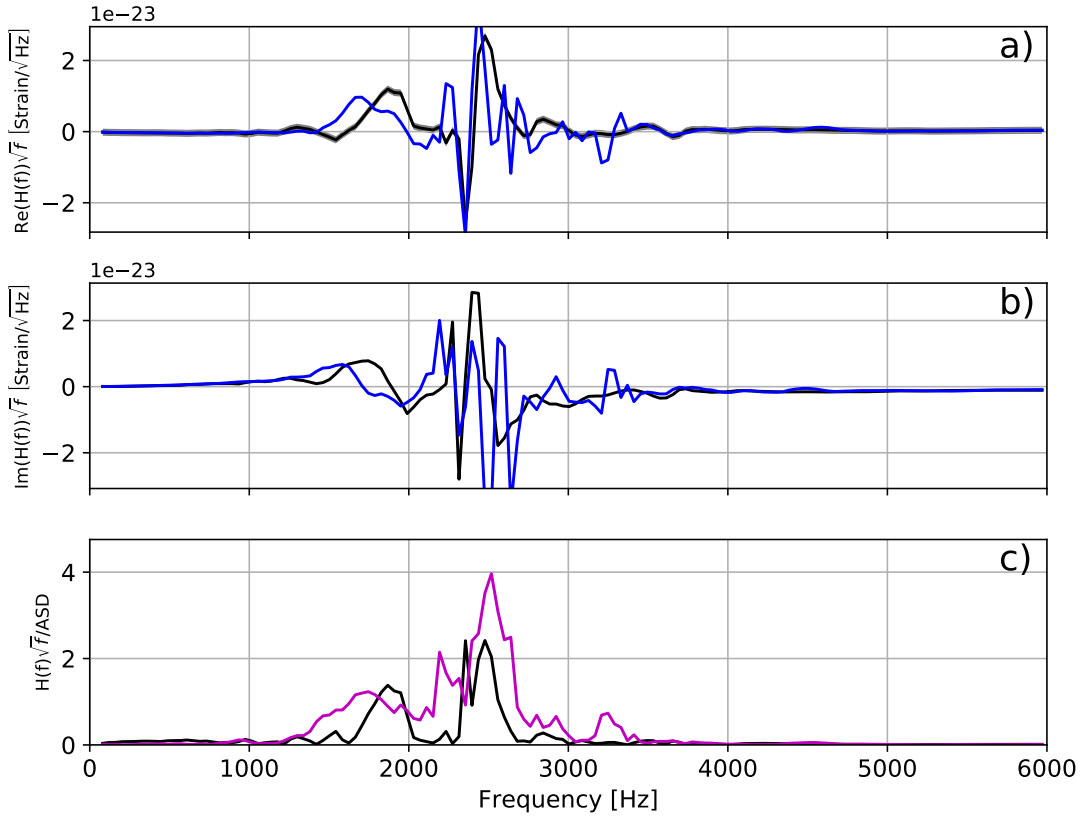


Figure 28: Complex frequency response of waveform ALF2-q10-M1225 and corresponding error signal when trained on the real and imaginary parts of the Fourier response using The Cannon 2 algorithm. The total SNR value for this signal is 2.33 and the residual SNR value is 2.57. Plot a) real part of the amplitude response multiplied by \sqrt{f} . The black trace is the original signal and the blue trace is the signal inferred from The Cannon 2 training on this signal without cross validation. Plot b) imaginary part corresponding to the signals shown in plot a). Plot c) residual SNR plot, the black trace is the magnitude of the signal multiplied by \sqrt{f} and divided by the advanced LIGO amplitude spectral density noise value. Values larger than one indicates parts of the signal that significantly contribute towards the detected LIGO SNR value. The pink trace shows the magnitude of the complex subtraction between the original signal and the inferred signal, scaled by \sqrt{f} and divided by the LIGO amplitude spectral density noise curve. Values larger than one significantly contribute to the residual SNR value.

Which coincidentally, also has a residual SNR of 2.57 with a previous residual SNR of 3.56 (figure 22) which is a slight decrease. The performance of these two sample signals when learning on the real and imaginary parts of the FFT, without leave one out cross-validation, is not significantly better than those trained in the log amplitude phase phase. Furthermore, implementing leave one out cross-validation would deteriorate these results further. At this point in time we considered looking at another learning algorithm, random forest regression, which is examined in section 6.4.

6.3 The Cannon 2 summary

When we trained the Cannon 2 on the amplitude and phase information (see section 6.2.1) we initially achieved reasonable results, however, this was when our waveform under test was

included in the training set. Machine learning algorithms are routinely tested with "out of sample" data, in other words, the signal under test should be excluded from the training data. When we excluded our test waveform from the training set (section 6.2.2) the residual SNR values increased dramatically to a range of values between 3 and 25 which is much too high for our application, where our goal is to achieve numbers much less than one for the residual SNR so that the reconstructed waveform is indistinguishable to the true waveform from the point of view of LIGO. We then altered our training method to train on the real and imaginary signals, to attempt to counteract any deterioration in performance due to phase errors. This did not result in any significant improvement. However, it must be noted that the training and prediction process for each waveform occur in a few seconds, so any future modifications that reduce the residual SNR are well worth implementing.

6.4 Random forest analysis

For implementation of the random forest regression algorithm, we decided to implement a simplified frequency shift in both the real and imaginary components of the Fourier transform. Rather than use the more complex frequency multiplication, which required interpolation of the signals, a frequency bin shifting algorithm was used (section 6.1.1). Leave one out cross-validation was not performed in this section as a method was required to calculate the frequency shift to reverse for a waveform excluded from training set, and this was a task set for future work. The initial random seed was kept fixed in this section.

6.4.1 Inferred waveforms

Figure 29 shows the waveform inferred from the random forest algorithm trained on the real and imaginary parts of the APR4/1.275M_⊙ with frequency bin shifting:

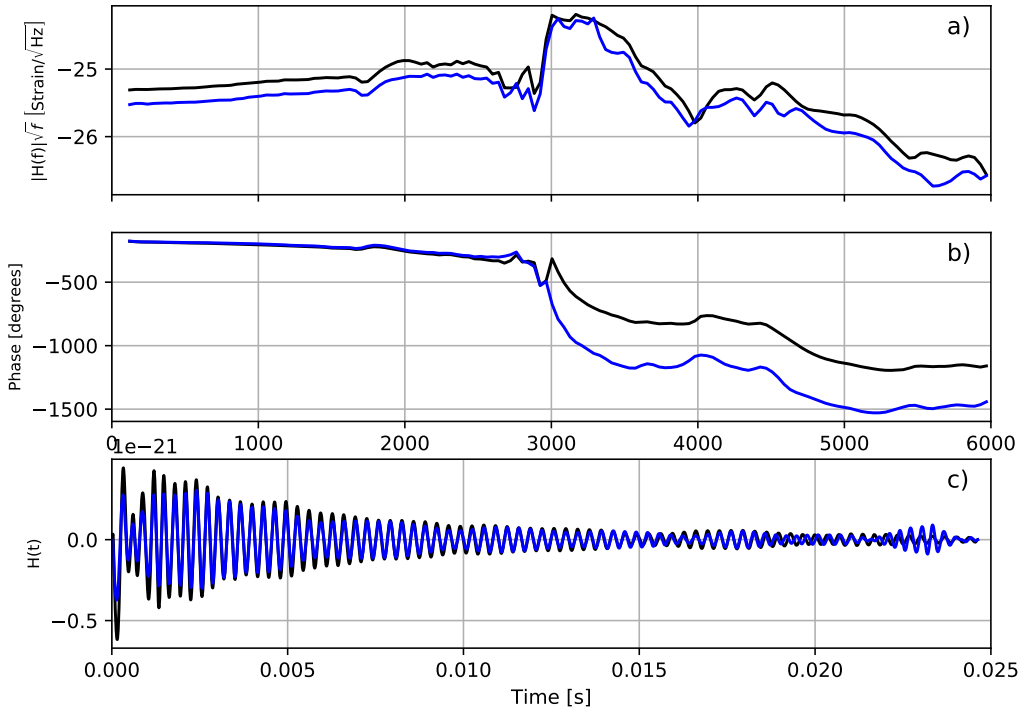


Figure 29: Frequency and time response of waveform APR4-q10-M1275 using random forest regression trained on the real and imaginary components of the waveforms using frequency bin shifting for alignment. The total SNR for this signal is 2.09 and the residual SNR is 0.71. These plots do not implement leave one out cross-validation. Plot a) is the calculated magnitude of the frequency response, the black trace is the original signal and the blue trace is the inferred signal. Plot b) is the calculated phase response, the original phase is the black trace and the inferred phase is blue. Plot c) is the time response of the signal with the original time series signal is the black trace, and the inferred signal is the blue trace.

The magnitude of the inferred signal in the frequency domain (blue curve plot a) is consistently lower than the original spectrum (black curve plot a), resulting in a time domain signal that underestimates the original signal. The zero crossing in the time domain of the

inferred waveform and original signal align well up to 18ms and loose synchronisation after this time. The inferred signal has a residual SNR of 0.71 which is reasonably low, but this does not include cross-validation. Looking now at the other signal, the random forest response to ALF2/1.225M_⊙ is shown in figure 30:

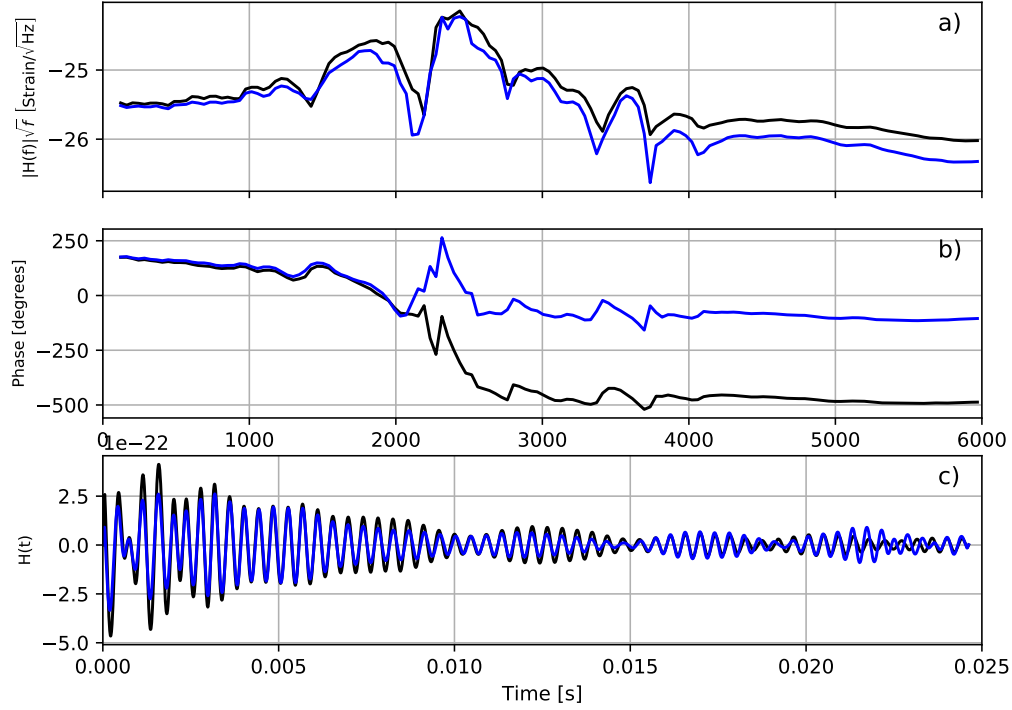


Figure 30: Frequency and time response of waveform ALF2-q10-M1225 using random forest regression trained on the real and imaginary components of the waveforms using frequency bin shifting for alignment. The total SNR for this signal is 2.34 and the residual SNR is 0.80. These plots do not implement leave one out cross-validation. Plot a) is the calculated magnitude of the frequency response, the black trace is the original signal and the blue trace is the inferred signal. Plot b) is the calculated phase response, the original phase is the black trace and the inferred phase is blue. Plot c) is the time response of the signal with the original time series signal is the black trace, and the inferred signal is the blue trace.

As with figure 29, the synchronisation in the time domain aligns well for time periods less than 18ms, but the amplitude of the time domain signal is consistently underestimated, particularly immediately after merger when the signal strength is largest. The residual SNR for this waveform is 0.80, slightly larger than APR4/1.276M_⊙. Now that the sample signals have been analysed, the residual SNR values can be determined for all the signals, this was calculated and shown in the histogram in figure 31:

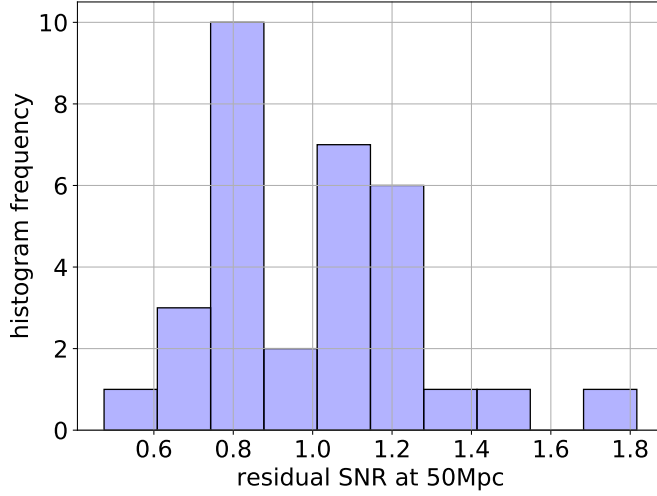


Figure 31: Histogram of the residual SNR for the random forest regression algorithm without cross-validation.

The residual SNR is less than 1.8 for all waveforms, though this was achieved without cross-validation. These values are still too high for our purposes as residual SNR values of less than 1.0 are required, and it should also be noted that a stronger signal will result in a larger residual SNR. Figure 31 has been generated from the random forest algorithm with a fixed random seed, the next figures investigate the effect of the random seed on the residual SNR values. Figure 32 shows the mean residual SNR when run with 100 different random seeds:

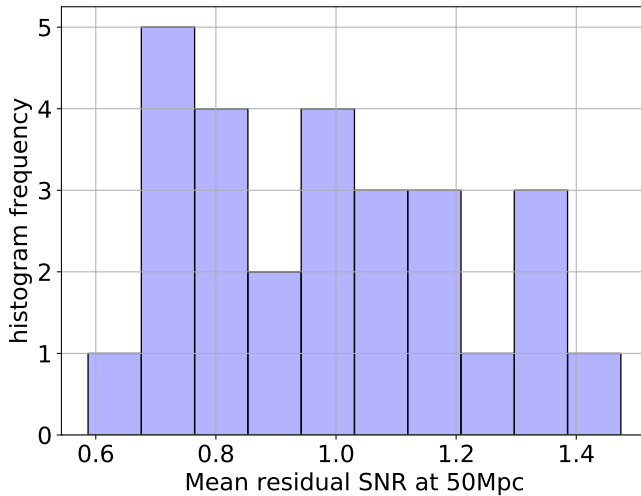


Figure 32: Mean histogram of the residual SNR for the random forest regression algorithm without cross-validation. There were a total of 100 different random seeds used to generate this plot.

The upper limit of the mean residual SNR is slightly less than the value obtained in figure 31, but otherwise the range of values is essentially the same, from 0.6 to 1.5, indicating that the random forest algorithm is relatively independent of the initial random seed chosen. This can be explored further by visualising the relationship of the random seeds on individual EOS/mass combinations as shown in figure 33:

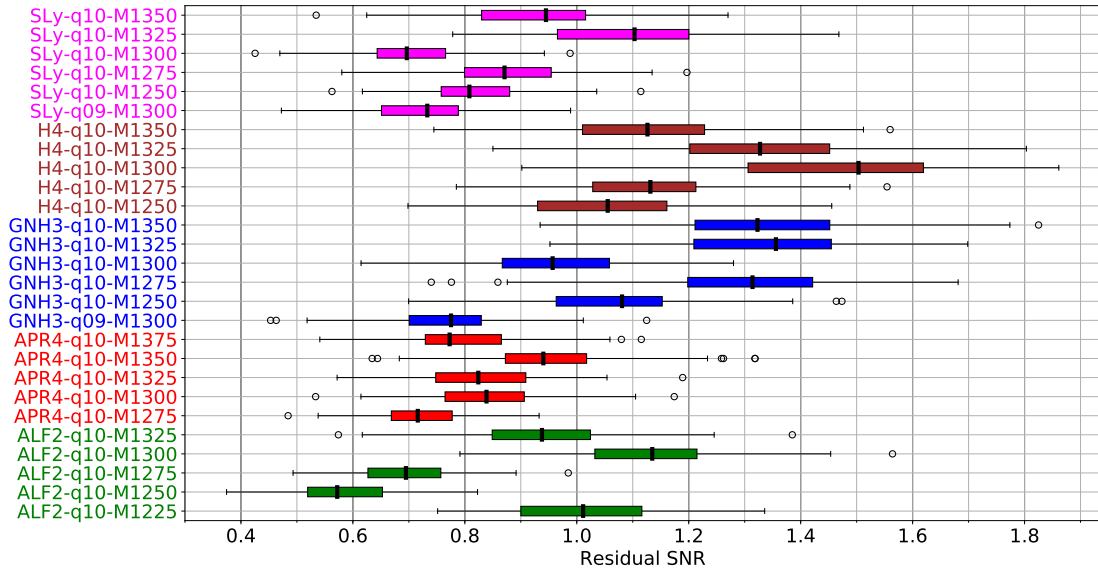


Figure 33: Box plot of the residual SNR for each waveform using random forest regression without cross-validation. The plots have been sorted by equation of state and mass combinations. The coloured box indicates the interquartile range, the thick vertical black line indicates the median value. The thin horizontal lines pass from the minimum value to the maximum values, excluding outliers. The outliers are indicated as round circles on the plot.

The box plot has been sorted by EOS and mass and coloured the same way as in figures 8 and 9. The residual SNR scores appear to be consistently distributed for each input waveform combination, though outliers (circles) do tend to appear occasionally. The variation of the residual SNR over the interquartile range is around ± 0.1 to ± 0.2 , whereas the variation over the minimum and maximum values, excluding outliers, varies up to ± 0.5 . If these waveforms were generated with cross-validation, it would be expected that the lowest and the largest mass values, for a given EOS would have a larger residual SNR due to the position on the extrema of the waveforms, though this is not generally the case here. It is also instructive to sort these values by the mean residual SNR and this is shown in figure 33:

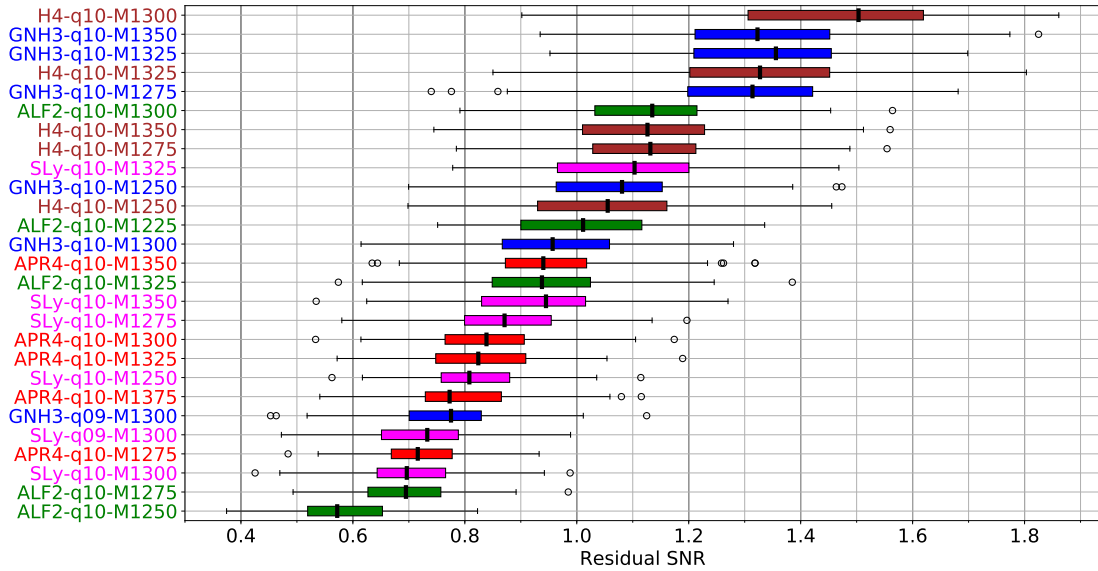


Figure 34: Box plot of the residual SNR for each waveform using random forest regression without cross-validation. The plots have been sorted by the mean value of the residual SNR. The coloured box indicates the interquartile range, the thick vertical black line indicates the median value. The thin horizontal lines pass from the minimum value to the maximum values, excluding outliers. The outliers are indicated as round circles on the plot.

This box plot shows the waveforms ranked by residual SNR for the random forest algorithm. This shows that ALF2/1.250M $_{\odot}$ is consistently the best match of all the waveforms, and that H4/1.300M $_{\odot}$ is consistently the worse match of all the waveforms. Comparison of figure 34 to the scaled PCA decomposition in figures 13-16 yields no obvious connection other than the worst four waveforms (H4-q10-M1325 to H4-q10-M1300 on this plot) tend to be outliers on the amplitude of the PCA space, but that is quite a weak relationship. This plot also shows where the test waveforms fall in terms of the other waveforms. APR-q10-M1275 has the fourth lowest residual SNR with a value of around 0.7, and ALF2-q10-M1225 is mid-ranged with a value of around 1.0. Both these values are consistent with previous results.

One particularly useful parameter available to random forest decision trees is the ability to ascertain which inputs were most important in determining the output waveforms. This parameter is known as the relative importance and is shown in figure 35.

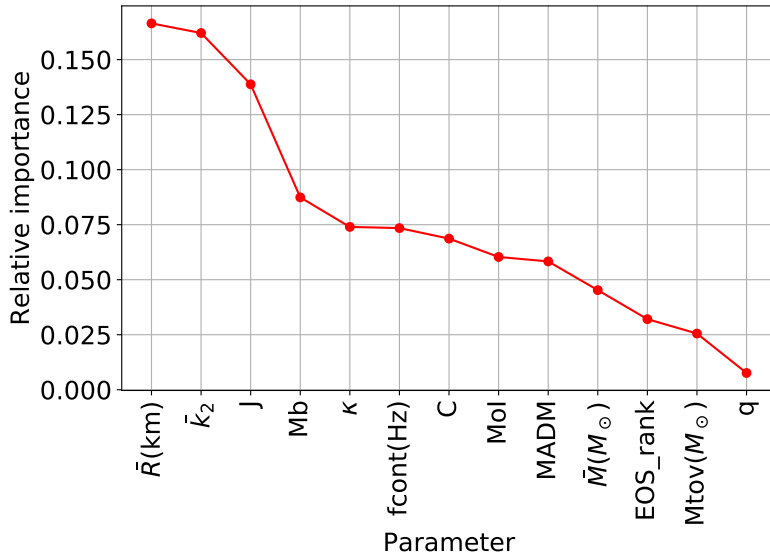


Figure 35: Sorted relative importance of labels for random forest decision trees without cross-validation. This plot indicates the relative importances for the reconstructed BNS progenitor gravitational wave properties in the decision making process of the random forest algorithm. Higher importance values indicate greater impact in determining the reconstructed output strain waveform. The three most important properties were found to be: the mean neutron star radius, \bar{R} ; the total angular momentum, J , at initial separation; and the dimensionless tidal number, \bar{k}_2 , at infinite separation.

Out of the thirteen input parameters for each waveform, 47% of the decisions made for signal generation was made with from the mean neutron star radius, \bar{R} , the Love 2 tidal parameter \bar{k}_2 and the initial angular momentum of the system J . It also is interesting to note from figure 35 that the neither of the three most important properties of the reconstruction include the EOS, or mass values. Nevertheless, the EOS properties are implicitly encoded in the mean neutron star radius and the tidal Love number, and the mass values are encoded in the initial angular momentum of the system.

6.4.2 Random forest summary

The random forest algorithm generated waveforms with lower residual SNR than The Cannon 2, however, at this point in time, cross-validation was not implemented in the random forest algorithm. Without cross-validation, the random forest regressor was able to create waveforms that were getting close to the required accuracy, with residual SNR values in the range of 0.6 to 1.5, but these values are still too large. The goal for the residual SNR value is less than one and this is dependent on the initial signal strength. The waveforms used in this thesis were normalised to a BNS event at 50Mpc, if the event occurred further out then a smaller residual SNR would be observed. The random forest algorithm was consistent due to variations in the initial random number seed, however, outliers were observed with maximum values for residual SNR that can exceed 1.8. The ratio of the residual SNR to signal SNR varied from 0.22 to 0.62, if the incoming signal SNR had a detectable value of 5.0 to allow detection, then to obtain a residual SNR of less than 1.0 requires that the ratio is less than 0.2 which is below the lower limit. These problems could possibly be related to the lack of test waveforms which leaves open the following question "How many waveforms do we need to get acceptable residual SNR" and this is a question for future work.

7 Future tasks

This project was performed with 25 numerical waveforms, this is a small amount for machine learning. It is possible that a significant improvement may occur in the predictions of The Cannon 2, and random forest, if more numerical relativity waveforms were used. The random forest algorithm could be modified to learn the frequency shift amount so that a full leave one out cross-validation process can be performed.

8 Conclusion

We investigated the possibility of using machine learning algorithms to generate a large bank of template waveforms to enable the post-merger detection of BNS, we use three types of machine learning analysis to investigate this possibility. The first algorithm was principal components analysis an unsupervised learning algorithm (section 6.1). We then investigated The Cannon 2, a supervised machine learning algorithm which used a form of L1 regularisation to predict outcomes, this algorithm was used without cross-validation (section 6.2.1) and with cross-validation (section 6.2.2). Finally, we used a random forest supervised machine learning algorithm without cross-validation (section 6.4).

The first algorithm used was principal components analysis which is an unsupervised learning algorithm. We projected this down into a three dimensional space and a two dimensional space to see if any intuitive findings could be obtained. We found that it was difficult to determine any visual correlation when frequency scaling was used, but without frequency scaling there was a visual correlation between the first principal component and the frequency corresponding to the peak spectral response for a given waveform.

The Cannon 2 algorithm performed reasonable well without leave one out cross-validation, but still had difficulty training to both the amplitude and phase. When leave one out cross-validation was implemented it performed quite poorly with residual SNR values around 3.0-25, when the desired result was a residual SNR of less than 1.0. Training on the real and imaginary parts of the spectra did not help the results and was not continued.

The signals generated from the random forest algorithm were quite promising, but we could not implement leave one out cross validation in the given time frame and further work is required. An algorithm has been generated to perform leave one out cross-correlation and can be used for future work. Finally, the computational time for these algorithms are a mere fraction of the computational time to generate numerical relativity waveforms. Furthermore, these waveforms may be required to be able to detect any post-merger remnant from the gravitational-waves of a BNS merger. It is therefore worth persevering on this task to generate BNS post-merger waveforms from machine learning.

It is also possible that by adding in more numerical relativity waveforms, we can achieve better results than has been specified here, and that should also be followed up in future work.

9 Acknowledgements

A big thank you goes to both my supervisors for all the time and effort you have put into this project. Another big thank you should go to my family as well who I have spent little time with over the last few months. And of course stack exchange for all those cryptic python problems.

References

- Abbott, B. P., Abbott, R., Abbott, T. D., et al. 2016a, Physical Review Letters, 116, 241103
- . 2016b, Physical Review Letters, 116, 61102
- Abbott, B. P., Abbott, R., Abernathy, M. R., et al. 2016c, Living Reviews in Relativity, 19, 1
- Abbott, B. P., Abbott, R., Abbott, T. D., et al. 2017a, Physical Review Letters, 118, 1
- . 2017b, Physical Review Letters, 119, arXiv:1709.09660
- Abbott, B. P., Abbott, R., Abbott, T., et al. 2017c, Physical Review Letters, 119, 161101
- Antoniadis, J., Freire, P. C. C., Wex, N., et al. 2013, Science, 340, 448
- Arnould, M., Goriely, S., & Takahashi, K. 2007, Physics Reports, 450, 97
- Arnowitt, R., Deser, S., & Misner, C. W. 1959, Physical Review, 116, 1322
- Baiotti, L., & Rezzolla, L. 2017, Reports on Progress in Physics, 80, 096901
- Bernuzzi, S., Dietrich, T., & Nagar, A. 2015, Physical Review Letters, 115, 1
- Breiman, L. 2001, Machine Learning, 45, 5
- Breu, C., & Rezzolla, L. 2016, Monthly Notices of the Royal Astronomical Society, 459, 646
- Caltech/MIT/LIGO Lab. 2015, ligo20150731e, url
- Carroll, S. M. S. 2004, Spacetime and geometry. An introduction to general relativity, Vol. 1 (Addison Wesley), 513, doi:10.1063/1.1881902
- Casey, A. R., Hogg, D. W., Ness, M. K., et al. 2016, arXiv, 1
- Clark, J. A., Bauswein, A., Stergioulas, N., & Shoemaker, D. 2015, Classical and Quantum Gravity, 33, 85003
- Demorest, P. B., Pennucci, T., Ransom, S. M., Roberts, M. S. E., & Hessels, J. W. T. 2010, Nature, 467, 1081
- Flanagan, E. E., & Hughes, S. A. 2005, arXiv, arXiv:0501041
- Lasky, P. P. D., Haskell, B., Ravi, V., Howell, E. J. E., & Coward, D. D. M. 2014, \prd, 89, 47302
- Lattimer, J. M., & Prakash, M. 2001, The Astrophysical Journal, 550, 426
- Narayan, R., Paczynski, B., & Piran, T. 1992, The Astrophysical Journal, 395, L83
- Owen, B. B. J., & Sathyaprakash, B. S. 1999, Physical Review D, 60, 22002
- Özel, F., & Freire, P. 2016, Annual Review of Astronomy and Astrophysics, 54, 401

- Pedregosa, F., Varoquaux, G., Gramfort, A., et al. 2011, Journal of Machine Learning Research, 12, 2825
- . 2017, Underfitting vs Overfitting
- Ravi, V., & Lasky, P. 2014, Monthly Notices of the Royal Astronomical Society, 441, 2433
- Read, J. S., Baiotti, L., Creighton, J. D. E., et al. 2013, Physical Review D, 88, 044042
- Read, J. S. J. J. S., Lackey, B. D. B. D., Owen, B. B. J., & Friedman, J. J. L. 2009, Physical Review D - Particles, Fields, Gravitation and Cosmology, 79, 1
- Rezzolla, L., Giacomazzo, B., Baiotti, L., et al. 2011, Astrophysical Journal, Letters, 732, L6
- Rezzolla, L., & Takami, K. 2016, Physical Review D, 93, 124051
- Ringnér, M. 2008, Nature Biotechnology, 26, 303
- Ruiz, M., Lang, R. R. N., Paschalidis, V., & Shapiro, S. L. S. 2016, Astrophysical Journal, Letters, 824, L6
- Shapiro, S., & Teukolsky, S. 2004, Black holes, white dwarfs and neutron stars: the physics of compact objects (John Wiley & Sons)
- Symbalisty, E., & Schramm, D. N. 1982, Astrophysical Letters, 22, 143
- Takami, K., Rezzolla, L., & Baiotti, L. 2015, Physical Review D, 91, 64001
- the Virgo Collaboration, t. V. 2017, GW170814 Sky Localisation
- Wall, M. E., Rechtsteiner, A., & Rocha, L. M. 2003, A practical approach to microarray data analysis, 44, 1